

Attoseconds and the exascale: on laser plasma surface interactions



Robin Timmis
Your College
University of Oxford

A thesis submitted for the degree of
Doctor of Philosophy

Michaelmas 2014

Acknowledgements

Personal Institutional

The author thanks the Norreys Research Group, Prof. Philip Burrows and Dr. Qingsong Feng for useful discussions, the SMILEI consortium and the ARCHER2 support team. The authors also acknowledge the support of AWE plc, UKRI-EPSRC and the Oxford-Berman Graduate Scholarship program. This work used the ARCHER2 UK National Supercomputing Service (<https://www.archer2.ac.uk>) under project e674 of URKI-EPSRC grant no. EP/R029148/1 and UKRI-STFC grant no. ST/V001655/1.

Abstract

The commissioning of multi-petawatt class laser facilities around the world is gathering pace. One of the primary motivations for these investments is the acceleration of high-quality, low-emittance electron bunches. Here we explore the interaction of a high-intensity femtosecond laser pulse with a mass-limited dense target to produce MeV attosecond electron bunches in transmission and confirm with three-dimensional simulation that such bunches have low emittance and nano-Coulomb charge. We then perform a large parameter scan from non-relativistic laser intensities to the laser-QED regime and from the critical plasma density to beyond solid density to demonstrate that the electron bunch energies and the laser pulse energy absorption into the plasma can be quantitatively described via the Zero Vector Potential mechanism. These results have wide-ranging implications for future particle accelerator science and associated technologies.

Contents

List of Figures	ix
A List of Symbols and Abbreviations	xi
1 The Zero Vector Potential Absorption Mechanism	1
1.1 Motivations and an overview	1
1.2 Introduction	3
1.2.1 ZVP electron bunch energies	10
1.2.2 ZVP bunches oblique incidence scaling	13
1.2.3 Defining characteristics of the ZVP mechanism	16
1.3 Numerical simulations of the ZVP mechanism	16
1.3.1 The ZVP mechanism in 3D3V	17
1.4 The ZVP electron bunch	23
1.4.1 Energy absorption in the ZVP regime	33
1.4.2 Unpacking the QED effects of Figure 1.12	35
1.4.3 Errors	38
1.5 Planned future work	39
1.6 Conclusions	43
Appendices	
A General plasma physics	47
A.1 Lorentz transformations of electromagnetic fields	47
A.2 The headlight effect	48
A.3 Geometric transverse emittance	48
B PIC simulations	51
B.1 Convergence of 3D PIC simulations	51
References	53

List of Figures

1.1	Diagram of a p-polarised laser pulse incident at angle θ specularly reflected from a solid density plasma.	5
1.2	Diagram of a <i>p</i> -polarised laser pulse incident on an ablating overdense plasma.	7
1.3	The numerical simulation using a 3D Particle-In-Cell (PIC) code of the Zero Vector Potential (ZVP) mechanism.	18
1.4	Propagation of a vector potential zero through the ablating ZVP electron bunch.	21
1.5	Electron dynamics in 3D PIC simulation for both linear and circularly polarised relativistic laser pulses.	22
1.6	The Fourier transform of the reflected laser pulse in 3D PIC simulations. .	23
1.7	2D PIC simulation results qualitatively describing typical mass-limited ZVP electron bunch structure.	25
1.8	Energy spectra for mass-limited electron bunches formed via linearly and circularly polarised laser pulses.	27
1.9	Mean mass-limited ZVP electron bunch normalised kinetic energies extracted from 2D PIC simulations.	29
1.10	Mass-limited electron bunch train length as a function of laser intensity and plasma density.	30
1.11	The relative errors for each mean energy data point compared to Figure 1.9.	33
1.12	Peak instantaneous bulk electron bunch total energy escaping to the plasma bulk rear.	34
1.13	An exploration of ZVP 2D PIC simulation stability.	38
1.14	Planned GEMINI-PW experimental setup for the measurement of ZVP electron bunches.	40
B.1	Comparison between the initial 3D simulation and a lower resolution version.	52

x

A List of Symbols and Abbreviations

Note All quantities are defined in SI units unless otherwise specified throughout the thesis.

α Twiss parameter = $-\frac{\langle x_i x'_i \rangle}{\epsilon_{\text{rms}}^i}$
a_0 Normalised vector potential = $\frac{e \mathbf{E}_L }{m_e c \omega_L}$
A Atomic mass number
\mathbf{A} Three-vector potential
\mathbf{A}^μ Four-vector potential = $(\phi/c, \mathbf{A})$
β Normalised speed = v/c or Twiss parameter = $\frac{\langle x_i \rangle}{\epsilon_{\text{rms}}^i}$
β Normalised velocity = \mathbf{v}/c
\mathbf{B} Magnetic field
\mathbf{B}_L Magnetic field of a laser pulse
c Speed of light = $3.00 \times 10^8 \text{ m s}^{-1}$
δ Skin depth
$\delta(\mathbf{x})$ Dirac-delta function
$d\mathbf{s}$ Vector line element
Δ Change in a variable
D Number of dimensions
∇ Partial derivative = $\hat{\mathbf{x}}_\mu \frac{\partial}{\partial x_\mu}$, $\mu = x, y, z$
ϵ_0 Permittivity of free space = $8.854 \times 10^{-12} \text{ F m}^{-1}$
ϵ_{rms} Transverse geometric emittance
$\epsilon_{n,\text{rms}}$ Transverse normalised emittance
e Absolute charge of an electron = $1.602 \times 10^{-19} \text{ C}$
e^\pm Electron (-) or positron (+)
\mathbf{E} Electric field
E_S Schwinger electric field = $1.3 \times 10^{18} \text{ V m}^{-1}$

E _L	Electric field of a laser pulse
<i>f</i>	Distribution function
F _L	Lorentz force = $q(\mathbf{E} + \mathbf{v} \times \mathbf{B})$
γ	Lorentz/gamma factor = $\frac{1}{\sqrt{1-\beta^2}}$ or Twiss parameter = $\frac{\langle x_i'^2 \rangle}{\epsilon_{\text{rms}}^i}$ or high-energy photon
η	Efficiency
<i>I</i>	Electromagnetic field intensity
\mathcal{H}	Hamiltonian
θ	Angle of incidence of a laser pulse
J	Current density
k	Electromagnetic three-wave vector
K ^{μ}	Electromagnetic four-wave vector = $(\omega/c\mathbf{k})$
<i>K</i>	Boltzmann constant = $1.38 \times 10^{-23} \text{ J K}^{-1}$
λ_D	Debye length $\equiv \sqrt{\frac{\epsilon_0 K T_e}{n_e e^2}}$
λ_L	Laser pulse wavelength
Λ_ν^μ	Lorentz transformation matrix
<i>L</i>	Length
\mathcal{L}	Lagrangian
μ_0	Vacuum permeability = $1.257 \times 10^{-6} \text{ N A}^{-2}$
<i>m</i> _e	Mass of an electron = $9.11 \times 10^{-31} \text{ kg}$
<i>n</i>	Harmonic order
<i>n</i> , <i>N</i>	Number
<i>n</i> _c	Plasma critical density = $\frac{\omega_L^2 m_e \epsilon_0}{e^2}$
<i>n</i> _e	Plasma electron number density
\bar{n}_e	Normalised plasma electron number density = $\frac{n_e}{n_c}$
<i>n</i> _i	Plasma ion number density
n	Vector normal to a surface
<i>N</i> _A	Avogadro's number
<i>N</i> _D	Number of particles within the Debye sphere = $\frac{4}{3}\pi\lambda_D^3 n$
ω	Angular frequency of an oscillation or low energy photon
ω_L	Laser pulse angular frequency

ω_p	Plasma frequency = $\sqrt{\frac{e^2 n_e}{m_e \epsilon_0}}$
ϕ	Angle of laser polarisation out of the plane of interaction or scalar electromagnetic potential
\mathbf{p}	Three-momentum
P	Pressure
\mathbf{P}^μ	Four-momentum = $(U/c, \mathbf{p})$
Q	Charge
ρ	Density
r_L	Relativistic Larmor radius = $\frac{\gamma m_e v}{e \mathbf{B} }$
\mathbf{r}	Radial vector
$\hat{\mathbf{r}}$	Radial unit vector
R	Rate
σ	Surface area
S	Relativistic similarity parameter = \bar{n}_e/a_0
$S(\mathbf{x})$	Shape function
τ	Average time or standard deviation of time
t	Time
T	Kinetic energy
T_e	Plasma electron temperature
u, v	Speed
\mathbf{u}, \mathbf{v}	Velocity
U	Energy
v_ϕ	Phase velocity
V	Potential or volume
w_L	Beam waist
w_p	Quasi-particle weight
χ_γ	Photon quantum parameter
x, y, z	Standard Cartesian coordinates in 3D
$\mathbf{x}, \mathbf{y}, \mathbf{z}$	Vectors along each axis of the Cartesian coordinate system
$\hat{\mathbf{x}}, \hat{\mathbf{y}}, \hat{\mathbf{z}}$	Unit vectors along each axis of the Cartesian coordinate system
Z	Ion charge state in units of e

Subscripts . . . The following are defined the subscripts

C	Pseudocapacitor
e	Electron
γ	Photon
L	Laser pulse or Longitudinal
T	Transvere to a laser pulse
pol	Along the polarisation vector of a laser pulse
\perp	Perpendicular
\parallel	Parallel
i, j	Indices
s	Species
x, y, z	Along the specific Cartesian axes
∞	

The hat symbol To represent a normalised vecotr

primed coordinates and reference frames

1D, 2D, 3D . . .	One-, two- or three-dimension(al)
BW	Breit-Wheeler
CLF	Central Laser Facility
CPA	Chirped Pulse Amplification
CSE	Coherent Synchrotron Emission
FDTD	Finite Difference Time Domain
HB	Hole Boring
HED	High-Energy-Density
HHG	High Harmonic Generation
HPC	High Performance Computing
OHREX	ORION High Resolution X-ray
PIC	Particle-In-Cell
QED	Quantum Electro-Dynamics
RR	Radiation Reaction
SF-QED	Strong-Field Quantum Electro-Dynamics
ZVP	Zero Vector Potential

1

The Zero Vector Potential Absorption Mechanism

Contents

1.1	Motivations and an overview	1
1.2	Introduction	3
1.2.1	ZVP electron bunch energies	10
1.2.2	ZVP bunches oblique incidence scaling	13
1.2.3	Defining characteristics of the ZVP mechanism	16
1.3	Numerical simulations of the ZVP mechanism	16
1.3.1	The ZVP mechanism in 3D3V	17
1.4	The ZVP electron bunch	23
1.4.1	Energy absorption in the ZVP regime	33
1.4.2	Unpacking the QED effects of Figure 1.12	35
1.4.3	Errors	38
1.5	Planned future work	39
1.6	Conclusions	43

1.1 Motivations and an overview

Throughout the history of experimental science, light has always been the primary tool of investigation and discovery. Through the creation of synchrotron radiation sources and more recently XFELs, electron bunches have been employed to create increasingly specialised light sources for the study of matter of all kinds. At

SLAC, the United States' forefront electron accelerator, applications hail from many disciplines: science, medicine, industry and homeland security. At Diamond Light Source, the UK's national synchrotron science facility, studies range from novel drugs to ancient paintings. Unsurprisingly, extensive research efforts have been enlisted to produce electron bunches of ever greater charge, energy and coherency. Multi-petawatt laser facilities are now available across the globe for the study of laser-plasma interactions in the ultra-relativistic regime $a_0 \gg 1$. Here, there is a novel method for high-charge electron bunch creation. Via relativistic effects, a laser pulse organises the electrons at the surface of a solid density plasma into coherent bunches that can be ejected at high speeds. Those discussed in this thesis have properties comparable to those of forefront accelerators but on ultra-short timescales. The quality, charge and duration of the attosecond electron bunches described here would enable the study of the most fundamental interactions of our universe. Electron bunch formation from solid targets has received much interest in recent years [1–8] with some experimental evidence for attosecond electron bunches from intense laser-solid interactions [9–11]. This interest stems partially from their ability to produce higher charge bunches at lower intensities compared to gas targets [9]. Here is proposed a new mass-limited target setup to generate electron bunches of extreme charge density. These electron bunches are fully characterised in 3D PIC simulations to compare their quality to those of existing electron bunch production methods. Their energies are described via an extended version of the ZVP Mechanism and the corresponding implications for laser to plasma energy absorption are also considered including the intersection of ZVP with Strong-Field Quantum Electro-Dynamics (SF-QED) effects of next generation laser facilities. ZVP theory has direct relevance to High Harmonic Generation (HHG) due to the known intrinsic link between electron bunches and the reflection mechanism [12, 13].

These results have excited the community to perform experiments to realise these electron bunches for the creation of ultra-bright X-ray pulses: after the recent successful campaign at the ORION laser facility, studying HHG from such electron

bunches, details are presented here for the upcoming experiment to observe the electron bunches directly at the GEMINI PW laser at the Central Laser Facility, UK.

This Chapter is organised as follows. Section 1.2 outlines the ZVP mechanism including quantitative calculations of system properties. In Section 1.3.1 the first 3D PIC simulations to observe the ZVP mechanism are presented. Further PIC simulations are presented in Section 1.4 focusing now on the hot electron bunches produced via the mechanism their properties, energy scalings and implications for SF-QED. Section 1.5 details the planned experiment to observe the ZVP mechanism at the GEMINI-PW laser facility including. Finally, concluding remarks are given in Section 1.6.

1.2 Introduction

Of primary interest in this thesis is the interaction of a relativistically intense short-pulse laser interacting with a solid density plasma target with a sharp density gradient. Now is presented one model for the interaction: the ZVP mechanism as proposed by *Baeva et al* [14] and later developed by *Savin et al* [13, 15]. Alongside the theories of the Relativistic Electron Spring [16] and Coherent Synchrotron Emission [17], ZVP is a post-ponderomotive model of attosecond absorption and reflection. The model considers a quasi-static surface equilibrium state analogously to ion acceleration in the hole boring [18] and light sail regimes [19].

An explanation for the absorption of laser energy into dense plasmas was first suggested by Wilks and Kruer [20]. A ponderomotive mechanism where plasma electrons are heated directly by the laser pulse via the $\mathbf{J} \times \mathbf{B}$ force. This thesis is interested in the so-called ‘post-ponderomotive’ regime where the frequency of relativistic plasma oscillations ($\omega_p \sim \sqrt{S}$) are greater than the $\mathbf{J} \times \mathbf{B}$ induced plasma electron oscillations at $2\omega_L$. The plasma electrons’ response is then fast enough to compensate the ponderomotive pressure of the laser pulse with the formation of electrostatic fields between electrons and ions and so respond adiabatically to the applied $\mathbf{J} \times \mathbf{B}$ force. Hence, plasma electrons cannot be heated directly by the laser pulse. Interestingly, this condition suggests a criterion for the ZVP regime, $S > 4$,

slightly more constraining than $S > 1$ as is typically stated for the ZVP regime [15]. The bulk plasma must have $S > 1$ to prevent relativistic transparency and so ensure a laser-surface interaction. Then the ponderomotive pressure of the laser will typically compress the front surface to densities such that the overdensity condition is satisfied, provided the target is of sufficient thickness. Note that to neglect the pre-adiabatic formation phase requires a sufficiently steep density gradient around the relativistic critical density surface (where $S = 1$) to shift the main interaction to a region where this condition on the overdensity is satisfied. Pre-plasma formation and scale length will be discussed in great detail in the following chapters. For now, assume the technology exists to control this phenomenon.

Provided all conditions are met, the ponderomotive pressure of the laser pulse compresses electrons at the front surface of the plasma and so shifts the laser-plasma surface interaction to plasma densities well beyond the relativistic critical density, leaving in its wake a positive space charge of ions. This electron-ion charge separation leads to the formation of a *pseudo-capacitor* electrostatic field. Having entered a regime of adiabaticity, the plasma skin layer is confined within a potential well consisting of the ponderomotive pressure of the laser pulse and the Coulomb potential of the pseudocapacitor field. Thus is formed a high density and longitudinally thin electron bunch (sometimes referred to as an electron sheath in the literature [16]) at the plasma surface.

To understand this system, consider now a relativistic linearly polarised laser pulse obliquely incident, at an angle of incidence θ , on a semi-infinite plasma, existing for $x \geq 0$ as in Figure 1.1.

The Hamiltonian of a single electron confined within the potential well [21] is

$$\mathcal{H} = c\sqrt{m_e^2c^2 + |\mathbf{p}|^2} - e\Phi. \quad (1.1)$$

Here, the second term of Equation 1.1 describes the contribution to the electron's energy from the electrostatic potential, Φ , of the pseudo-capacitor. The first term is the electron energy, U , extracted from the invariant of the relativistic 4-momentum

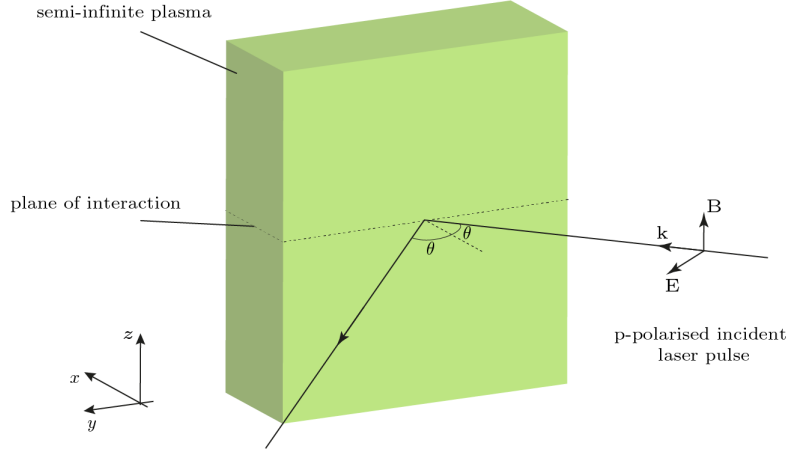


Figure 1.1: Diagram of a p-polarised laser pulse incident at angle θ specularly reflected from a solid density plasma. By considering the Lorentz force equation, it is clear that all forces and therefore all plasma particle dynamics are confined to a plane.

of the electron, $\mathbf{P}^\mu = (U/c, \mathbf{p})$,

$$\mathbf{P}_\mu \mathbf{P}^\mu = \frac{U^2}{c^2} - |\mathbf{p}|^2 = m_e^2 c^2. \quad (1.2)$$

Decomposing the electron's 3-momentum into orthogonal components: p_{prop} , along the laser propagation direction, p_{pol} , along the polarisation axis of the laser pulse and p_\perp , perpendicular to both, there are two simplifications to be made. Firstly, by canonical conservation of transverse momentum, $p_{\text{pol}} = eA$, where A is the laser vector potential amplitude. Secondly, in the case of a p-polarised laser pulse (the known optimum for ZVP electron bunch generation [13] and HHG [22]), with reference to Figure 1.1 and the Lorentz force law, the forces at play confine the electron trajectory to the $p_{\text{prop}}-p_{\text{pol}}$ plane and the essential interaction geometry is two-dimensional. This is provided one considers length scales smaller than the focal spot of the laser pulse on the target, such that variation of the ponderomotive pressure with the third dimension can be neglected.

Explicitly, the Hamiltonian can be written as

$$\mathcal{H} = c\sqrt{m_e^2 c^2 + p_{\text{prop}}^2 + e^2 A^2} - e\Phi. \quad (1.3)$$

From Equation 1.3 it is clear that should the vector potential pass through zero, one of potential well walls is totally suppressed, enabling electrons in the skin layer

to escape the plasma, breaking adiabaticity. The necessity of vector potential zeros for this violent reconstruction of the plasma surface led Baeva *et al* [14] to coin the term ‘Zero Vector Potential’ mechanism to describe this process. Indeed, while elementary electromagnetism tells us a laser pulse will exponentially decay within a skin layer of a plasma without passing through zero, Baeva *et al* [14] demonstrated in PIC simulations that in this non-linear regime, zeros do exist and do propagate through the skin layer. The explanation relies on a Doppler shift in the laser field due to the relativistic motion of the ablating plasma surface, and a mathematical formalism of this process proceeds as follows.

As the ZVP mechanism is a relativistic phenomenon, it is absolutely essential to perform a relativistic analysis. Since all accelerated electrons travel at approximately speed c , surface electrons undergo similar trajectories. Acting collectively they oscillate in the laser pulse field. Consider first a transformation to the frame of reference where the laser pulse is normally incident to the plasma surface, this frame travels at velocity $\mathbf{v} = (c \sin \theta) \hat{\mathbf{y}}$ with electrons streaming at $-\mathbf{v}$. Using Equation 1.2, $U = \gamma m_e c^2$ and integrating Equation ?? in the boosted frame noting $p_T(t = 0) = \gamma_{\mathbf{v}} m_e v = m_e c \sin \theta \cos \theta$,

$$\gamma^2 = 1 + (a_0 + \sin \theta \cos \theta)^2 + \left(\frac{p_{\text{prop}}}{m_e c} \right)^2, \quad (1.4)$$

where all parameters are in the boosted frame. Using $\mathbf{p} = \gamma m_e \mathbf{v}$, the longitudinal velocity is

$$v_{\text{prop}} = \frac{\tilde{p}_{\text{prop}} c}{\sqrt{1 + (a_0 + \sin \theta \cos \theta)^2 + \tilde{p}_{\text{prop}}^2}}, \quad (1.5)$$

where $\tilde{p}_{\text{prop}} = p_{\text{prop}}/m_e c$. Thus, should the transverse vector potential pass through $-\sin \theta \cos \theta$, zero for normal incidence, the surface can propagate towards the laser pulse at very close to speed c . Transforming back to the laboratory frame, at the peak of ablation ($\mathbf{u} \approx -c \hat{\mathbf{x}}$) and using the equations for relativistic velocity addition,

$$\mathbf{u}'_{\parallel} = \frac{\mathbf{u} - \mathbf{v}}{1 - \mathbf{u} \cdot \mathbf{v}/c^2}, \quad (1.6)$$

$$\mathbf{u}'_{\perp} = \frac{\mathbf{u}_{\perp}}{\gamma_v (1 - \mathbf{u} \cdot \mathbf{v}/c^2)}, \quad (1.7)$$

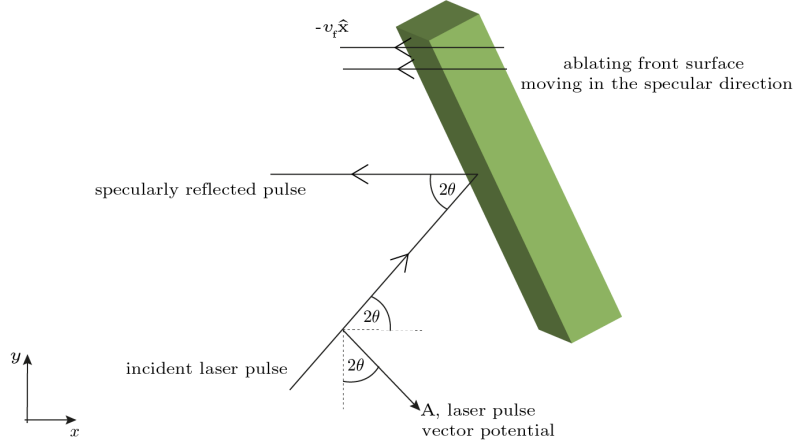


Figure 1.2: Diagram of a p -polarised laser pulse incident on an ablating overdense plasma. The laser is incident obliquely at an angle of θ and is reflected specularly. The plasma ablates specularly also. The interaction geometry is confined to a 2D plane.

where $\gamma_v = 1/\sqrt{1 - |\mathbf{v}|^2/c^2}$ [23], one finds that this peak ablation at speed $\approx c$ occurs now in the specular reflection direction. Simultaneity is broken and ripples co-move along the surface with the incident laser pulse wavefronts.

Transform now to the rest frame of the ablating front. Beyond the relativistic critical density surface, the vector potential of the laser pulse decays evanescently. At the spatial centre of the laser pulse, it can be described simply by

$$\mathbf{A}'_{\text{L}}(t', r') = A'_0 \cos(\omega'_{\text{L}} t') \exp(-r'/\delta') \hat{\mathbf{r}}'_{\text{pol}} = A'_0 \hat{\mathbf{r}}'_{\text{pol}}, \quad (1.8)$$

where the primed symbols indicate that these quantities are measured in the rest frame of the expanding front. A'_0 is the vector potential amplitude and ω'_{L} is the frequency of the laser pulse, r' is the propagation distance of the laser into the plasma, δ' is the skin depth and $\hat{\mathbf{r}}'_{\text{pol}}$ a unit vector defining the polarisation direction of the laser pulse. Un-primed coordinates will indicate the lab frame measurements.

While previous demonstrations of the existence of vector potential zeros assumed that the ablation occurs normal to plasma surface, it is necessary to confirm that zeros are still predicted for specular ablation. Consider a p -polarised laser pulse confined to the x - y plane incident with an angle of incidence θ on an ablating overdense plasma expanding with velocity $-v_f \hat{x}$ in the lab frame, as in Figure 1.2.

The direction of polarisation is

$$\hat{\mathbf{r}}_{\text{pol}} = \hat{\mathbf{x}} \sin 2\theta - \hat{\mathbf{y}} \cos 2\theta \quad (1.9)$$

and the velocity of the rest frame of the ablating front relative to the lab frame is $-v_f \hat{\mathbf{x}}$.

Applying the Lorentz transformation to the electromagnetic 4-potential, \mathbf{A}^μ , where Λ_μ^ν is given by Equation ??, immediately from the y -coordinate transformation,

$$A'_L \cos 2\theta' = A_L \cos 2\theta. \quad (1.10)$$

Applying the headlight effect for a source moving at an angle 2θ to the boosted frame (a full derivation is given in Appendix A.2),

$$\cos(2\theta') = \frac{\cos(2\theta) - \beta}{1 - \beta \cos(2\theta)} \quad (1.11)$$

and rearranging Equation 1.10, the vector potential in the lab frame is

$$A_L = \frac{1 - \beta \sec(2\theta)}{1 - \beta \cos(2\theta)} A'_0 \cos(\omega'_L t') \exp(-r'/\delta'). \quad (1.12)$$

Writing the boosted frame space-time coordinates in terms of the lab frame coordinates,

$$ct' = \gamma(ct - \beta x), \quad (1.13)$$

$$x' = \gamma(x - \beta ct), \quad (1.14)$$

yields

$$A_L = A_0 \cos(\omega_L t - kx) \exp\left(-\frac{\sqrt{(x - \beta ct)^2 + (y/\gamma)^2}}{\delta}\right), \quad (1.15)$$

where

$$A_0 = \frac{1 - \beta \sec(2\theta)}{1 - \beta \cos(2\theta)} A'_0, \quad (1.16)$$

$$\omega_L = \gamma \omega'_L, \quad (1.17)$$

$$k = \frac{\beta \gamma \omega'_L}{c}, \quad (1.18)$$

$$\delta = \frac{\delta'}{\gamma}. \quad (1.19)$$

The oscillatory term in Equation 1.15 demonstrates the propagation of vector potential zeros within the plasma target. From the structure of this term it

would appear that these zeros are expelled from the plasma along the specular direction at a speed

$$v_\phi = \frac{\omega_L}{k} = \frac{c}{\beta} = -\frac{c^2}{v_f}. \quad (1.20)$$

While in their original ZVP paper Baeva laid some doubt on their version of this calculation, instead suggesting similarity theory predicts zeroes propagate at speed c [14], the theory of High Harmonic Generation rejects this alternative. It is well known that the emission of reflected radiation occurs primarily at the point where the transverse vector potential passes through zero [12] but equally that the width of the radiated pulse depends on the advance time emission point [24]. If the zeroes moved at speed c , then the observed emitted pulse would be infinitely thin, producing radiation with perfect coherence in all cases. This is unphysical and simulations have suggested finite advanced time bunch widths decreasing rapidly with increasing laser intensity [24]. This is precisely what is predicted by Equation 1.20. As the laser intensity increases, v_f naturally increases. Thus, the zeroes propagate closer to the speed of light and reducing the advanced time bunch width.

To summarise, for a sufficiently intense laser pulse, electrons at the surface of an irradiated solid target are accelerated by the laser to relativistic velocities at a fraction of a laser pulse cycle and therefore electrons both follow similar trajectories and respond adiabatically to the $\mathbf{J} \times \mathbf{B}$ force of the laser pulse. They form into a high charge density spatially thin coherent electron bunch on the front surface of the plasma but displaced inwards from the approximately immobile ions via the ponderomotive pressure of the laser. This charge separation generates a longitudinal electrostatic pseudocapacitor field that confines electrons to a potential well on the front surface of the plasma, preventing further propagation of the electron bunch into the plasma bulk. When the zero of the vector potential passes through the electron bunch, the ponderomotive pressure instantaneously vanishes and electrons are ejected specularly from the target, co-propagating with the zeroes of the vector potential.

In the work by Cousens *et al* on electron trajectories in this regime, it is noted that a Coherent Synchrotron Emission (CSE) radiation burst occurs when the transverse momentum goes to zero [cousens2020], corresponding to the passage of the zero of the transverse vector potential. CSE and ZVP are therefore intrinsically linked, however, while CSE focuses on reflection and the HHG spectrum, ZVP is concerned with laser pulse energy absorption.

After expulsion from the plasma, the pseudocapacitor is discharged as the electron bunch accelerates across it. Upon encountering the subsequent laser pulse peak amplitude, the bunch is then rotated back towards the plasma and launched into the bulk at high energy along the laser propagation axis (by conservation of transverse momentum in the plasma bulk), as it does so emitting coherent synchrotron radiation in transmission.

1.2.1 ZVP electron bunch energies

In [14], Baeva *et al* propose energy scalings in one-dimension (1D) for an electron bunch produced in the ZVP regime as a function of the incident laser pulse intensity and plasma density. This was extended to three-dimensions (3D) by Savin *et al* [13]. What follows is that discussion with closer consideration of both the constants of proportionality and their consequences. Note that throughout the electron bunch is treated as infinitessimally thin, as proved to be a reasonable assumption in previous work on ZVP [13, 22, 25]. Sub-bunch dynamics have been explored in more detail by Gonoskov *et al* [26].

The expressions for energies in equations 1.26 and 1.29 require the electron bunch to fully discharge the pseudo-capacitor before interaction with the subsequent laser pulse peak. Since the electron bunch travels at speed $\approx c$, the peak displacement (and thus the pseudo-capacitor width) must satisfy

$$\Delta x \leq \frac{\lambda}{8}. \quad (1.21)$$

Using Equation 1.24, it is clear Equation 1.21 is satisfied for $S \geq 1.3$ at normal incidence.

Consider again the semi-infinite block of plasma presented in Figure ??, normally irradiated by a laser pulse with wavelength λ_L and peak electric field, E_L . It is now the ponderomotive pressure of the laser that displaces the electron fluid in this picture. The electron surface moves inwards until the pressure exerted by the peak instantaneous ponderomotive pressure of the laser pulse cycle,

$$\mathbf{P}_L = \epsilon_0 E_L^2 \hat{\mathbf{x}} = \epsilon_0 \left(\frac{a_0 \omega_L m_e c}{e} \right)^2 \hat{\mathbf{x}} \quad (1.22)$$

is equal and opposite to the pressure exerted by the pseudo-capacitor field,

$$\mathbf{P}_C = \frac{QE_C}{\sigma} \hat{\mathbf{x}} = -\frac{(en_e \Delta x)^2}{\epsilon_0} \hat{\mathbf{x}} \quad (1.23)$$

from equations ?? and ?. Equating the magnitudes of \mathbf{P}_L and \mathbf{P}_C , the maximum displacement inwards of electrons is

$$\Delta x \hat{\mathbf{x}} = \frac{c}{\omega_L} \frac{a_0}{\bar{n}_e} \hat{\mathbf{x}} = \frac{1}{kS} \hat{\mathbf{x}}, \quad (1.24)$$

where k is the wave-vector of the laser pulse. Correspondingly,

$$E_C = \frac{en_e}{\epsilon_0} \Delta x = \frac{\omega_L c m_e a_0}{e} = E_L. \quad (1.25)$$

Applying the results of equations 1.24 and 1.25, when the ponderomotive pressure vanishes and the electron bunch is launched across the pseudo-capacitor, the relativistic kinetic energy gained by a single electron is

$$T = \int \mathbf{F} \cdot d\mathbf{s} = \int_{\Delta x}^0 -eE_C dx = \int_{\Delta x}^0 -\frac{en_e x}{\epsilon_0} dx = \frac{1}{2} m_e c^2 \frac{a_0^2}{\bar{n}_e} \quad (1.26)$$

or an electron gamma factor,

$$\gamma = \frac{1}{\sqrt{1 - \beta^2}} = 1 + \frac{a_0^2}{2\bar{n}_e}. \quad (1.27)$$

Assuming all displaced electrons are captured by the potential well and launched as a coherent bunch, the total number of electrons in the bunch is

$$N_e = n_e \sigma \Delta x = \frac{\sigma a_0 n_c}{k} = \sigma \epsilon_0 E_L \quad (1.28)$$

and hence, the total kinetic energy of the electron bunch is

$$U_{ZVP} = N_e T = \frac{\sigma n_c}{k} \times \frac{1}{2} m_e c^2 \frac{a_0^3}{\bar{n}_e}. \quad (1.29)$$

It is now interesting to compare Equation 1.29 to the laser energy deposited upon the plasma surface and therefore consider what fraction of the laser energy can be absorbed via the ZVP mechanism. Using $E_C = E_L$, Equation 1.29 can be rewritten as

$$U_{\text{ZVP}} = \frac{1}{2\omega_L S} \sigma c \epsilon_0 E_L^2. \quad (1.30)$$

For the case of normal incidence, bunches are produced at a frequency of $2\omega_L$, naturally following the frequency of the $\mathbf{J} \times \mathbf{B}$ force. Assuming a sinusoidal plane wave incident with surface area σ , the energy available during the pushing phase (a quarter-cycle) is

$$U_{L,1/4} = \sigma \frac{T}{4} \langle I_L \rangle = \frac{2\pi}{8\omega_L} \sigma c \epsilon_0 E_L^2. \quad (1.31)$$

Hence,

$$\eta_{\text{ZVP}} = \frac{U_{\text{ZVP}}}{U_{L,1/4}} = \frac{2}{\pi S}. \quad (1.32)$$

Interestingly, this analytical result predicts the trend observed by A. Savin [15] in PIC simulations both in magnitude and in scaling. Indeed, A. Savin demonstrated in numerical simulation

$$\eta_{\text{ZVP}} \sim S^{-1.000(3)}, \quad (1.33)$$

however, this result led A. Savin to conclude that increasing S reduces absorption, increasing the energy in the reflected HHG beam thus increasing high harmonic efficiency, seemingly in tension with the results of other works [16, 24]. The resolution arises from awareness of two distinct conversion efficiencies that describe the reflected harmonic spectrum: the total conversion efficiency into the full reflected beam and the conversion efficiency for individual harmonics. While the overall conversion into the reflected beam decreases for decreasing S , the slope of the harmonic spectrum becomes shallower and HHG efficiency increases. Indeed, high harmonic efficiency necessitates high reflection inefficiencies due to the production of ZVP electron bunches as higher energy bunches produce more coherent reflected radiation [24]. Harmonic efficiencies will be discussed in more detail in the following

Chapters, however, at currently accessible laser intensities, it would appear that X-ray harmonics are produced with greater efficiency for high S [27], a regime generally neglected in parameter scans given the computational and experimental challenges of accessing it.

Unfortunately, it is not possible to link the energy scaling derived in this Section to CSE since the harmonic emission occurs before the ZVP acceleration phase. In Dromey *et al*, the CSE regime was demonstrated for the first time in transmission through thin foils, however laser pulses are now of sufficient intensity to access CSE in reflection from solid targets. This has been identified as a more efficient approach if it can be reached due to the production of higher density and shorter duration electron bunches and therefore brighter and more coherent CSE [28].

1.2.2 ZVP bunches oblique incidence scaling

This section is inspired by ideas from the work of Gonoskov *et al* [16] and Vincenti *et al* [18] to extend the theory of the ZVP mechanism for energy absorption to the more practical¹ case of oblique incidence.

Provided the plasma-vacuum boundary is sufficiently steep, the plasma electrons will respond adiabatically to the laser pulse and arrange themselves to form a pseudocapacitor longitudinal electric field E_C at the plasma surface. At all points in this adiabatic ‘pushing’ phase, the surface electrons will be in a quasi-static equilibrium *i.e.* there will be a balance between the electromagnetic forces on them. Consider again the laser pulse incident on a solid density plasma existing for $x > 0$ at angle θ . Transforming to the frame of reference in which the laser is normally incident (quantities in this frame are indicated by the primed symbol), the electron and ion bulk plasma species stream at velocity $\mathbf{v}_d = -c \sin \theta \hat{\mathbf{y}}$. Applying the Lorentz force law along the longitudinal direction ($\hat{\mathbf{x}}$), for a displacement of the electron fluid x'_e (one assumes that the expression for a single electron at the surface describes the surface since all electrons follow similar trajectories), travelling at speed \mathbf{v}' ,

$$-e(\mathbf{v}'(x'_e) \times (\mathbf{B}'_L(x'_e) + \mathbf{B}'_i(x'_e)) \cdot \hat{\mathbf{x}} + E'_C(x'_e)) = 0, \quad (1.34)$$

¹Not only is this more feasible in experiment but has been shown to optimise HHG [16].

where the laser magnetic field,

$$B'_L = \frac{m_e \omega'_L a_0 \sin(\omega'_L t' - k' x'_e)}{e} \hat{\mathbf{z}} \quad (1.35)$$

and B_i is the magnetic field generated by the uncompensated ion current, $\mathbf{J}_i = Z n'_i(x'_e) \mathbf{v}_d$, where the electron fluid has been displaced. As before, from Equation ??,

$$E'_C = \frac{en'_e x'_e}{\epsilon_0}. \quad (1.36)$$

Applying Maxwell-Ampère's Law, Equation ??, and noting that by symmetry there can be no variation in the magnetic field with y' or z' , it becomes clear that

$$-\frac{d(\mathbf{B}'_i)_{z'}}{dx'} = \mu_0 (\mathbf{J}_i)_{y'}. \quad (1.37)$$

Integrating Equation 1.37 from $-\infty$ to x'_e , noting that $\mathbf{B}_i = 0$ at infinity and assuming a constant density profile n'_i for $x > 0$ with $Z n_i = n_e$,

$$\mathbf{B}'_i(x'_e) = \mu_0 en'_e x'_e c \sin(\theta) \hat{\mathbf{z}}. \quad (1.38)$$

Using equations 1.35, 1.36 and 1.38 and making the reasonable approximation that the relativistic electrons on the surface move at speed $v'_y \approx \pm c$ at peak displacement ($x'_e = x'_p$), 1.34 can be written as

$$-e \left(\pm c \left(\pm \frac{m_e \omega'_L a_0}{e} + \mu_0 en'_e x'_p c \sin \theta \right) + \frac{en'_e x'_p}{\epsilon_0} \right) = 0. \quad (1.39)$$

For the laser to be in the pushing phase, the first term must be negative, corresponding to \mathbf{v}' and \mathbf{B}'_L having the opposite sign, hence,

$$c \left(-\frac{m_e \omega'_L a_0}{e} \pm \mu_0 en'_e x'_p c \sin \theta \right) + \frac{en'_e x'_p}{\epsilon_0} = 0, \quad (1.40)$$

where here the \pm tracks the sign of \mathbf{v}' . After some manipulation, one arrives at

$$x'_p = \frac{1}{k' S' (1 \pm \sin \theta)}. \quad (1.41)$$

Transforming back to the lab frame,

$$x_p = \frac{\cos^2 \theta}{k S (1 \pm \sin \theta)}. \quad (1.42)$$

Convincingly, this reduces to Equation 1.24 for $\theta = 0$ and predicts the suppression and enhancement of the two surface oscillations per laser pulse cycle. Explicitly, for a laser pulse propagating at $y = x \tan \theta$, the peak displacement of the electron surface is enhanced for \mathbf{B}_L in the $+\hat{\mathbf{z}}$ -direction and suppressed for \mathbf{B}_L in the $-\hat{\mathbf{z}}$ -direction.

Again, integrating to find the work done as the electron bunch accelerates across the pseudocapacitor,

$$T(\theta) = \int \mathbf{F} \cdot d\mathbf{s} = \frac{1}{2} m_e c^2 \frac{a_0^2}{\bar{n}_e} \frac{\cos^4 \theta}{(1 \pm \sin \theta)^2}. \quad (1.43)$$

While it was to be expected that a component of the electric field acting into or out of the plasma would change the magnitude of the displacement, this result suggests that increasing the angle of incidence can increase the electron energy gain in the enhanced cycle more than the decrease in the suppressed cycle. Note that this is to be expected as it is known that HHG efficiency is improved for non-zero angle of incidence [16, 24]. It would be interesting to explore whether the presence of an external magnetic field could be applied to mimic the effect of oblique incidence by replacing the magnetic field due to the uncompensated ion current.

While this model would suggest an optimal angle for electron energy and therefore of HHG of $\pi/2$, if $\theta > \pi/4$, then, if the relativistic electron bunch is travelling at c along the specular reflection direction, the subsequent laser peak amplitude will never ‘catch up’ with the electron bunch, and electrons can escape, generating high charge electron bunches in reflection as observed in experiment by Lin *et al* [9], but reducing the efficiency of HHG.

Finally, the total bunch energy as a function of θ ,

$$U_{ZVP}(\theta) = \frac{\sigma n_c}{k} \times \frac{1}{2} m_e c^2 \frac{a_0^3}{\bar{n}_e} \frac{\cos^6 \theta}{(1 \pm \sin \theta)^3}. \quad (1.44)$$

As anticipated, oblique incidence can increase laser absorption efficiency for higher S plasmas which are currently more easily accessed compared to the more optimal low S plasmas.

1.2.3 Defining characteristics of the ZVP mechanism

In her original paper on the ZVP mechanism, T. Baeva *et al* [14] outlined 6 defining characteristics of the ZVP mechanism, namely,

1. The existence of vector potential zeros moving through the skin layer in the laboratory frame;
2. The existence of zeroes in the incident laser pulse vector potential required for the formation of fast electron bunches;
3. The generation of fast electron bunches with ultra-short temporal duration;
4. That such fast electron bunches follow the energy scalings of equations 1.26 and total energy 1.29;
5. Injection of the fast electron bunches is along the propagation axis of the laser pulse;
6. There must be an intrinsic link between the fast electron bunches and coherent HHG;

with the moving zeros within the skin layer being the key delineator between this post-ponderomotive regime of laser pulse energy absorption and all other proposed mechanisms. While such observational requirements are far beyond the reaches of current experimental know-how, numerical simulations in both 1- [14] and 2-dimensions [13] have confirmed the above points. Now is presented the first 3D simulations attempting to demonstrate these criteria.

1.3 Numerical simulations of the ZVP mechanism

This thesis relies on the analysis of 1,2 and 3D PIC simulations, primarily using the massively-parallel and open-source simulation code Smilei [29]. Simulation parameters are provided throughout.

1.3.1 The ZVP mechanism in 3D3V

3D simulation results are presented in Figure 1.3 alongside comparison to an equivalent 2D simulation. Simulation parameters are given in Table 1.1, such parameters are compatible with the 10 PW ELI-NP state-of-the-art short pulse laser facility [30] incident on foam targets. Figure 1.3c) clearly demonstrates the existence of high energy density electron bunches propagating through the plasma bulk in the direction of the laser pulse. Note that this ZVP criterion is a direct consequence of conservation of transverse momentum inside the plasma bulk where the laser fields cannot propagate. Figure 1.3b) shows these bunches escape to the rear of the bulk but lose energy as they do so. Looking now at Figure 1.3e) and the internal structure of the plasma bulk. These bunches drive two-stream and filamentation instabilities [31]. The bulk propagating electron bunches are accompanied by higher density electron bunches to either side of the plasma block with the side of emission alternating every half laser pulse cycle.

Considerations and convergence of 3D simulations

The plasma specifications were chosen to minimise computational load while ensuring numerical convergence, requiring over 100 billion macroparticles. The electron temperature is raised significantly higher than that which would be expected in such a laser-plasma system so as to resolve the Debye length. Anticipated plasma temperatures are calculated using 1D HYADES simulations in the following Chapter. While this temperature is unphysical and will lead to some small plasma expansion over the course of the simulation (negligible on these timescales), the temperature remains small compared to that imparted to the electron bunches by the laser pulse. The striking similarity between the 2 and 3D simulation results is a natural consequence of the 2D nature of the interaction geometry. It is, however, still reassuring to show that previous work withstands the test of reality's geometry and the simple elegance of the ZVP mechanism is not lost in the chaos.

For the 3D simulations only, particles were initialised randomly not regularly to avoid numerical error. Regularly initialised plasma blocks in 3D simulations

1.3. Numerical simulations of the ZVP mechanism

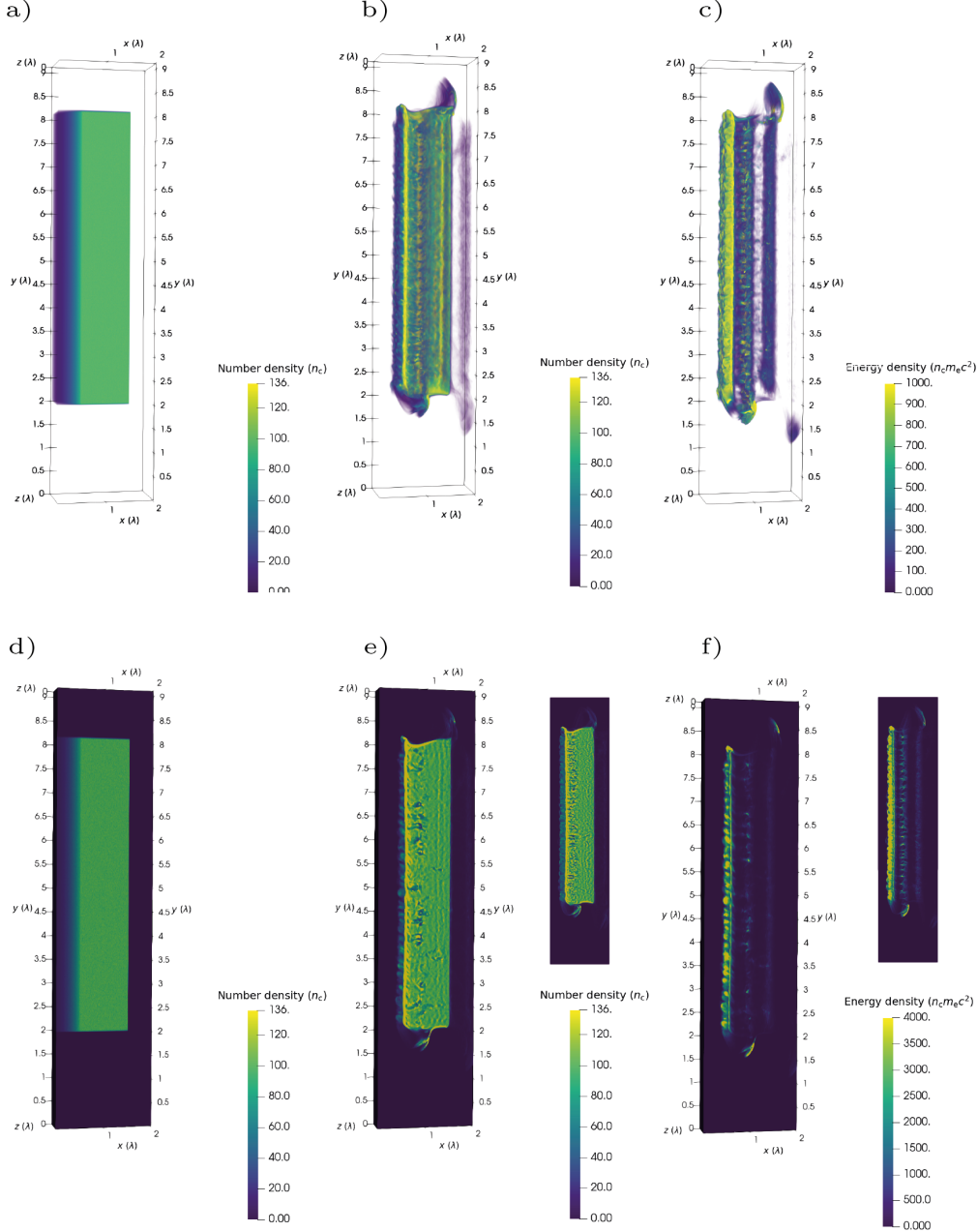


Figure 1.3: Simulation results from a 3D PIC simulation of the ZVP mechanism. a) The initialised electron number density. b) The electron number density several cycles later, the plasma bulk is intact, however there is evidence of instabilities and electron bunches propagating through and around the plasma. c) The electron kinetic energy density at the same timestep. Note that the scale has been clipped to enable observation of both electron bunches propagating through and around the plasma bulk. Significantly higher energy density, corresponding to a higher charge density and attosecond duration is observed for the electron bunches propagating around the bulk. d-f) Plots clipped through $z = \lambda_L/2$ for a-c) respectively for to access the internal structure of the plasma bulk. The accompanying plots for figures e) and f) are equivalent 2D PIC simulations demonstrating excellent agreement.

Laser (3D, normal incidence)		
Parameters	Real	Smilei
Wavelength, λ (nm)	1060	2π
Angular frequency, ω_L (fs $^{-1}$)	1.8	1
Beam waist, w_L (nm)	6λ	12π
Focal point, (x_f, y_f, z_f) (nm)	$(0.5\lambda, 5\lambda, 0.5\lambda)$	$(\pi, 10\pi, \pi)$
Spatial envelope, E_i , $i = y, z$	$E_i \sim e^{-(i-i_f)^2/w_L^2}$	
Temporal envelope, E_t	$E_t \sim e^{-(t-4\lambda/c)^2/((4\lambda/3c)^2 \ln 2)}$	
Simulation box		
Size, $x \times y \times z$ (nm)	$2\lambda \times 9\lambda \times \lambda$	$4\pi \times 18\pi \times 2\pi$
Sim length (fs)	35.22	20π
Spatial resolution, Δx (nm)	$\lambda/128 = 8.28$	0.0491
Temporal resolution, Δt (as)	$\Delta x/11c = 2.51$	0.00446
Collisionless, pre-ionised randomly-initialised aluminium plasma		
Electron x profile, $n(x)$	$\begin{cases} n_e & \text{for } 2\lambda \leq x \leq 3\lambda, \\ n_e e^{(x-2\lambda)/0.2\lambda} & \text{for } x \leq 2\lambda. \end{cases}$	
Electron y profile, $n(y)$	$\begin{cases} 1 & \text{for } 2\lambda \leq y \leq 8\lambda, \\ 0 & \text{otherwise.} \end{cases}$	
Electron z profile, $n(z)$	$\begin{cases} 1 & \text{for } 0.125\lambda \leq z \leq 0.875\lambda, \\ 0 & \text{otherwise.} \end{cases}$	
Ion profile, $n_i(x, y, z)$	$n_i = n(x)n(y)n(z)/13$	
Macro-electrons per cell	729	
Macro-ions per cell	8	
Ion temperature, T_i (keV)	0	0
Electron temperature, T_e (keV)	10	0.02
Stability criteria		
$\lambda_D/\Delta x$	0.288	
$1/\Delta t \omega_p$	24.4	
$\Delta x/c\Delta t$	11	
Macro-particles in the Debye sphere	210	

Table 1.1: Simulation parameters in both real and normalised Smilei simulation units for the 3D3V simulations.

rapidly blow apart due to spurious large amplitude fields generated on the large plasma surfaces due to macroscopic electron-ion charge separation at initialisation. 2D simulations with randomly initialised particles tend to produce nano-structures reminiscent of the cosmic web. The absence of these structures in 3D is telling. Unsurprisingly this error can be reduced by increasing the plasma temperature.

The longitudinal thickness of the target does not impact the interaction and is chosen for computational efficiency, indeed it is standard to consider such targets of thickness $\geq \lambda_L$ as bulk targets [32], however, for sufficiently long pulse durations, the effect of hole boring necessitates thicker targets to make this approximation as is necessary in the following Chapter.

The initial 3D simulation parameters were chosen to be consistent with previous work on the ZVP mechanism, however, such simulations are cumbersome. In order to query the defining characteristics outlined by Baeva, a lower resolution simulation was performed with similar parameters to the initial simulation. Comparisons between the simulation outputs are made in Figure B.1 in Appendix B.1. Good convergence is qualitatively demonstrated by the presence of characteristic features of the ZVP mechanism. While the instabilities are similar in structure, the change in seeding changes their exact positions. As instabilities are not the focus of this thesis this variation is of no cause for concern.

Confirmation of ZVP in 3D

Figure 1.4 tracks the transverse momentum distribution along the polarisation axis of the laser pulse of an electron bunch during its ablative journey, clearly demonstrating the existence of a singular zero of the vector potential propagating through the electron bunch and away from the plasma bulk. The zero propagates at a speed of $\approx 1.4c$, corresponding to a surface velocity of $\approx 0.71c$. In this simulation, the zero propagates through the bunch over a few nanometres and before crossing the pseudocapacitor. Note that consideration of the moving zeroes reframes the problem of the advanced time bunch width [24] (the determiner of attosecond CSE

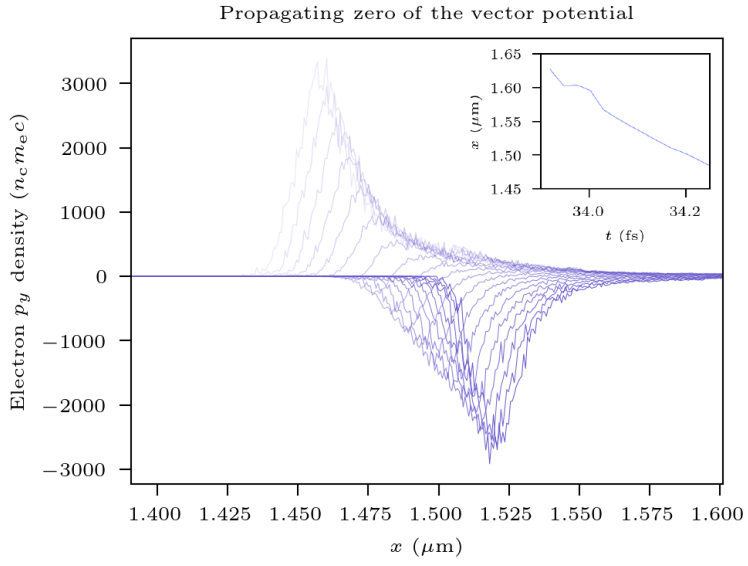


Figure 1.4: Propagation of a vector potential zero through the ablating ZVP electron bunch via the proxy of transverse momentum conservation. The zero of the vector potential exists where the transverse momentum is macroscopically zero. Each line represents a timestep with time increasing with decreasing colour. With increasing time the bunch and the zero move in the $-\hat{\mathbf{x}}$ -direction with the zero overtaking the electron bunch. The inset tracks the position of the zero of the vector potential with time.

pulse duration). Gonoskov *et al* have determined a scaling for electron bunch width [16] thus the only unknown is the surface velocity.

Further simulation results are presented in Figure 1.5. In Figures 1.5a)-d), comparisons are made in the electron energy distributions for simulations with zeros present in the vector potential (linearly polarised) and without (circularly polarised). Clearly zeroes are required for the formation of high energy, short duration attosecond bunches. From Figure 1.5a) it is clear that electron bunches are injected and propagate through the plasma bulk in the laser propagation direction. Figure 1.5c) demonstrates the quasi-monoenergeticity of the high energy electron bunches as initially identified in 1D by Baeva. Although the shape in the phase space is more complex in 3D, the attosecond duration at a given energy is retained. Figures 1.5e) and f) describe the surface dynamics in the linearly polarised case. One can observe the high density bunches on the front surface with the peak in energy density occurring after acceleration across the pseudocapacitor.

1.3. Numerical simulations of the ZVP mechanism

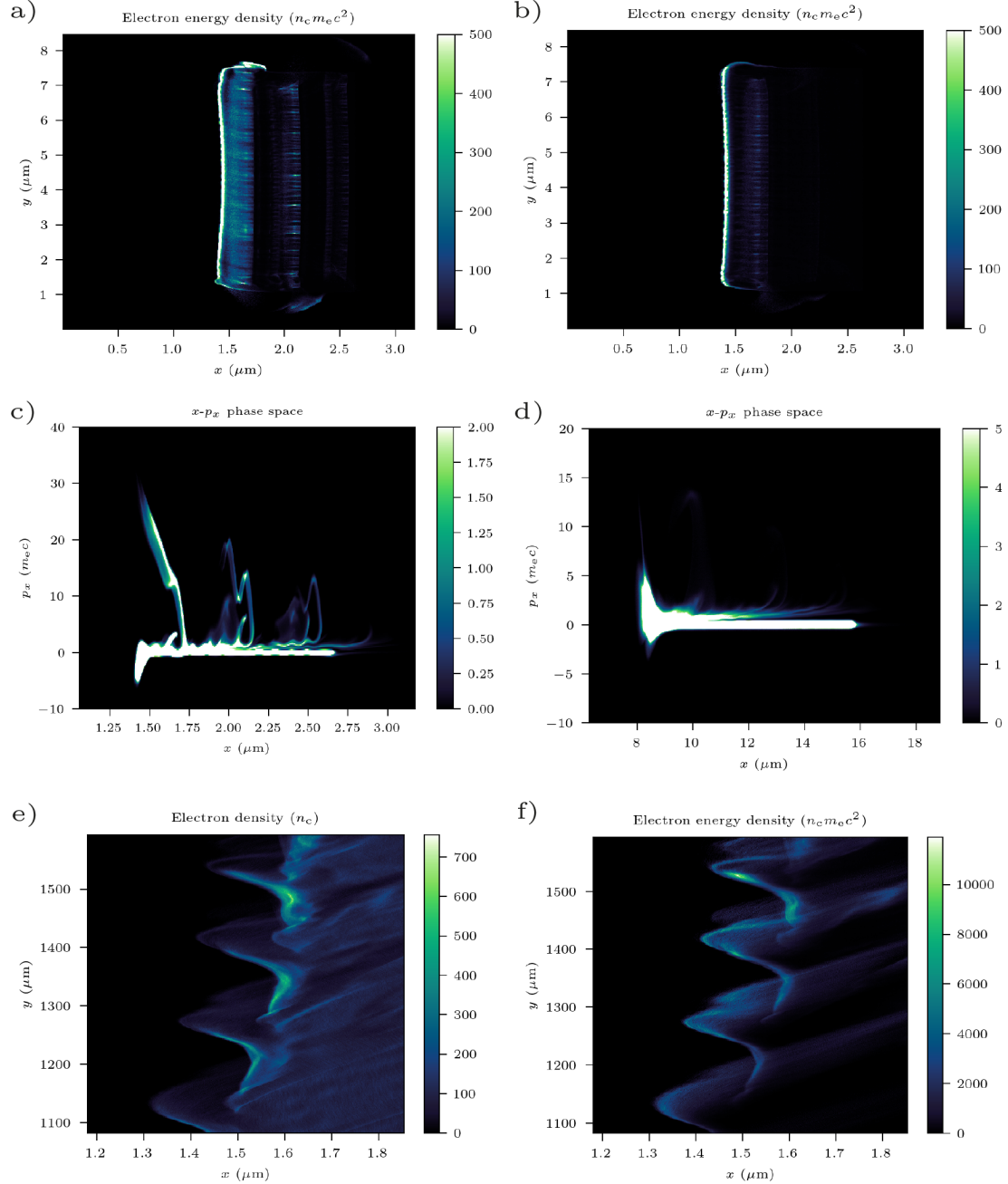


Figure 1.5: Electron dynamics in a 3D PIC simulation. a) and b) Electron energy density for linearly and circularly polarised laser pulses respectively. c) and d) Electron longitudinal momentum for linearly and circularly polarised laser pulses respectively. e) Electron density at the plasma surface streaked in time. f) Electron energy density at the plasma surface streaked in time.

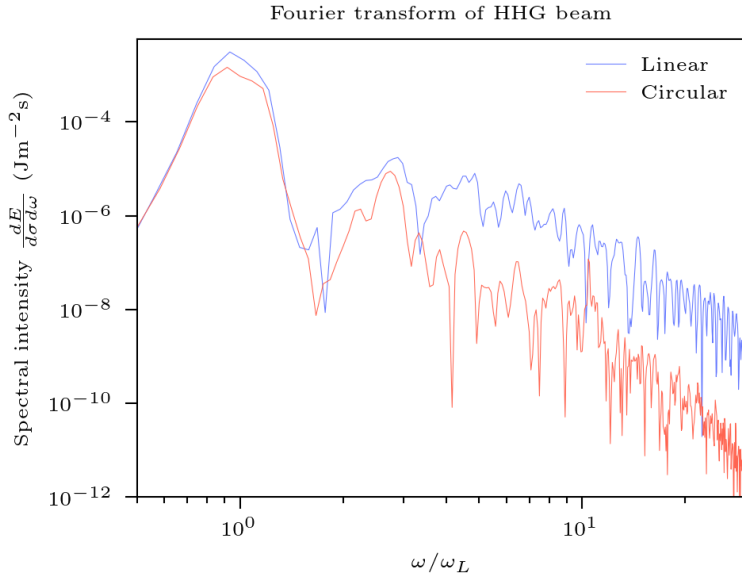


Figure 1.6: The Fourier transform of the reflected laser pulse in 3D PIC simulations both with and without zeroes in the vector potential.

Finally, Figure 1.6 compares the spectra of the reflected light in the presence and absence of zeros of the vector potential. Individual harmonics are not resolved due to blueshifts between successive pulse cycles from considerable hole boring, a phenomenon discussed in great detail in the following Chapter. The spectrum from the circularly polarised light is typically over two orders of magnitude below that for linearly polarised light. Thus, all defining characteristics of the ZVP mechanism have been identified in 3D simulations with the notable exception of the energy scalings. Next generation supercomputers will be required to perform such parameter scans.

1.4 The ZVP electron bunch

Following the excellent agreement demonstrated between 2 and 3D PIC simulations, the remainder of this Chapter explores ZVP primarily in 2D. Previous work on the ZVP mechanism has highlighted the high energy and short duration of electron bunches, what follows is a full characterisation of their properties. A ZVP electron bunch is an electron bunch produced via the ZVP mechanism. Once produced and accelerated across the pseudocapacitor field, it is launched back in the laser propagation direction. While the bunch has no spatial separation over energies

when propagating with the zero of the vector potential, the turning point of the electrons is longitudinal momentum dependent due to the Coulomb attraction of the ions after overshooting the pseudocapacitor field. Baeva *et al* showed that the electron bunch has a quasi-monoenergetic spectrum: the electron bunch is now of attosecond duration in the spectro-temporal domain and there is a one-to-one relationship between energy and position with the higher energies trailing the lower energies. The full bunch is confined to 130 as while a single energy confined to 5 as. If, however, the plasma bulk is transversely mass-limited relative to the laser spot size, when rotated back towards the plasma block, some of the electron bunch will overshoot and escape the potential well without significant chirping of the bunch as can be seen in Figure 1.3. Such electron bunches retain their high charge density and ultra-short duration with the tradeoff of increased divergence. Note that electron bunch properties are imprinted in the transmitted harmonics: high divergence but attosecond duration.

ZVP electron bunches can therefore be placed into two categories: ultra-high charge, ultra-short duration electron bunches from mass-limited targets, hereafter labelled mass-limited electron bunches, of interest due to their unique properties, and bulk propagating bunches, hereafter labelled bulk bunches, which have lower charge densities, are imprinted with instabilities and are instead of interest due to their connection to energy absorption and reflection in this post-ponderomotive regime. To investigate these two bunch types further, 2D PIC simulations were performed, see the Appendix for parameters.

Attosecond nano-Coulomb mass-limited electron bunches

The plots of Figure 1.7 describe a typical mass-limited ZVP electron bunch qualitatively. The electron bunch under interrogation is ultra-relativistic with a mean energy of 51(11) MeV and a duration of 35 as. It propagates at an angle of -0.393 rad relative to the laser propagation direction, *i.e.* the x -axis, and has a transverse geometric emittance in the simulation plane (the x - y plane) of 35(7) nm rad. The calculation of the transverse geometric emittance, a measure

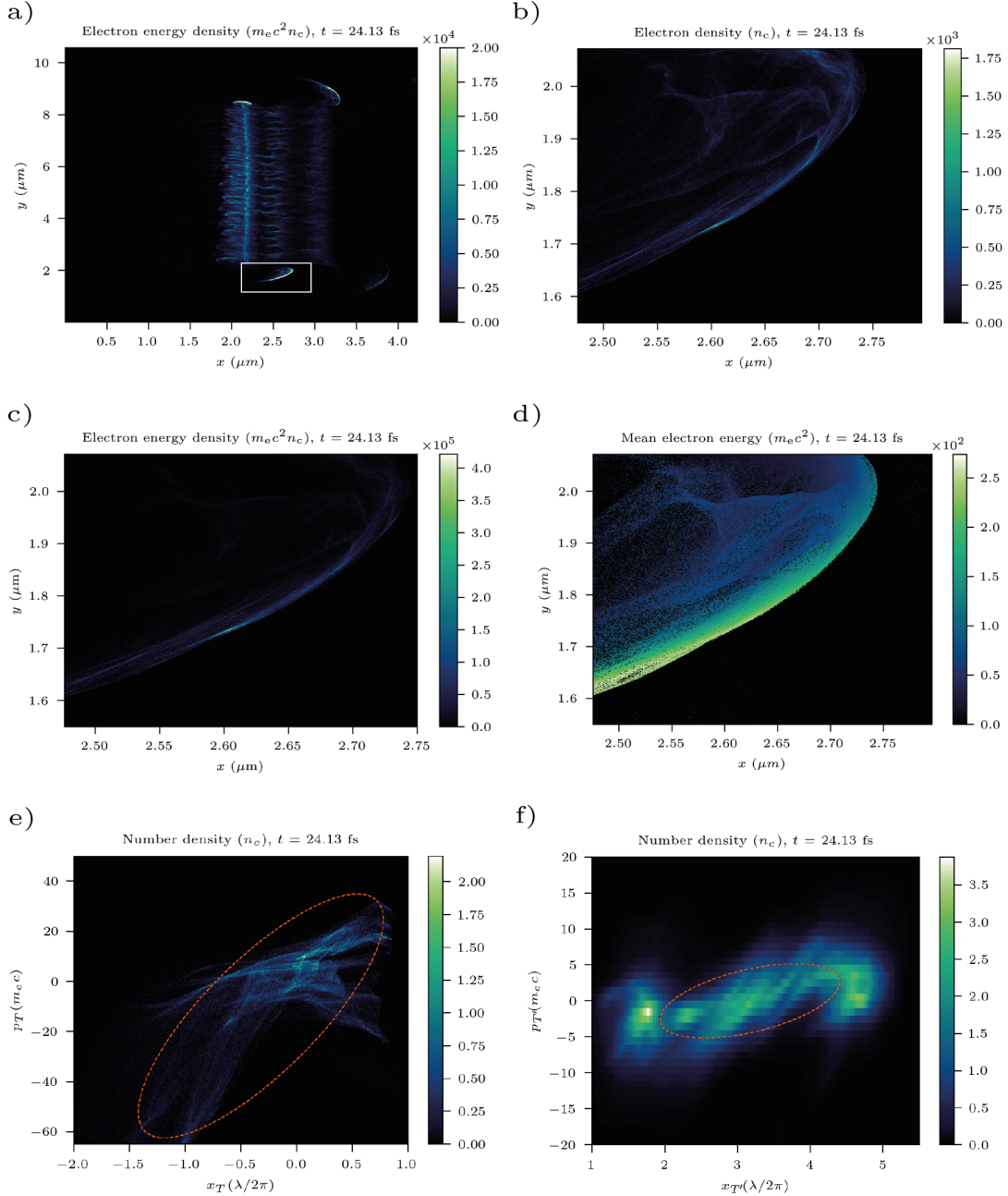


Figure 1.7: 2D PIC simulation results qualitatively describing typical mass-limited ZVP electron bunch structure. a) Electron energy density for the full simulation window, corresponds to Figure 1.3f). The box highlights the bunch presented in the following plots. b) Electron number density of the electron bunch. c) Electron energy density of the electron bunch, the colourbar scale has been increased compared to Figure a) to observe the internal structure. d) The mean electron energy across the electron bunch, suggesting a position dependent energy or quasi-monoenergetic nature to the electron bunch [14]. Cells with no macroparticles are black. e) The transverse phase space in the 2D simulation plane. The ellipse describes the calculated emittance. The skew of the ellipse is a consequence of a low density tail on the phase space beyond the bottom left corner. f) This plot was extracted from the equivalent 3D simulation and describes the transverse emittance in the z -direction. Again the ellipse marks the emittance. The relatively well-defined border to the phase space and the mild tilt (indicating only mild divergence) are direct consequences of the 2D nature of the interaction.

of the quality of the electron beam, is given in Appendix A.3. Note that while the bunch does not propagate in the laser propagation direction, this does not mean it must be rejected under consideration of the ZVP bunch conditions. We must expand the definition of a ZVP electron bunch. In the mass-limited case, a bunch must propagate at some angle to the laser due to conservation of canonical momentum while it remains in the thrall of the laser pulse. For an equivalent bunch in a corresponding 3D simulation, the transverse geometric emittance in the z plane is $15(11)\text{ nm rad}$. This electron bunch has a total charge of 0.35 nC for a slab of plasma of thickness 0.75λ in the z -direction. Note again the two-dimensional nature of the interaction geometry. Electrons a distance less than twice the relativistic Larmor radius,

$$r_L = \frac{\gamma m_e v}{e|\mathbf{B}|} \quad (1.45)$$

will escape to the side of the target when rotated back towards the plasma. Here, γ and v correspond to the electron velocity. The total number of electrons in the mass-limited bunch is

$$N = 2n_e r_L L_z \Delta x, \quad (1.46)$$

where L_z is the width of the plasma in the z -direction. Combining Equations 1.45 and 1.46 with 1.24 and 1.27 and taking $v \approx c$ for the ultra-relativistic electron bunch,

$$N \approx 2\gamma n_c \frac{L_z}{k^2}. \quad (1.47)$$

Equation 1.47 can be rewritten in terms of fundamental constants as

$$N \approx 2(1 + 0.5 \frac{a_0^2}{n_e}) L_z \frac{m_e \epsilon_0 c^2}{e^2}. \quad (1.48)$$

For these simulation parameters, this corresponds to a total bunch charge, $Q = eN$, of 0.37 nC , a remarkably successful prediction of the ZVP model. Perhaps counter-intuitively, it would appear the total charge scales inversely with the plasma density. Instead, charge can be increased either by increasing the laser pulse intensity or L_z . Indeed, provided the laser pulse intensity remains relativistic, the focal spot can

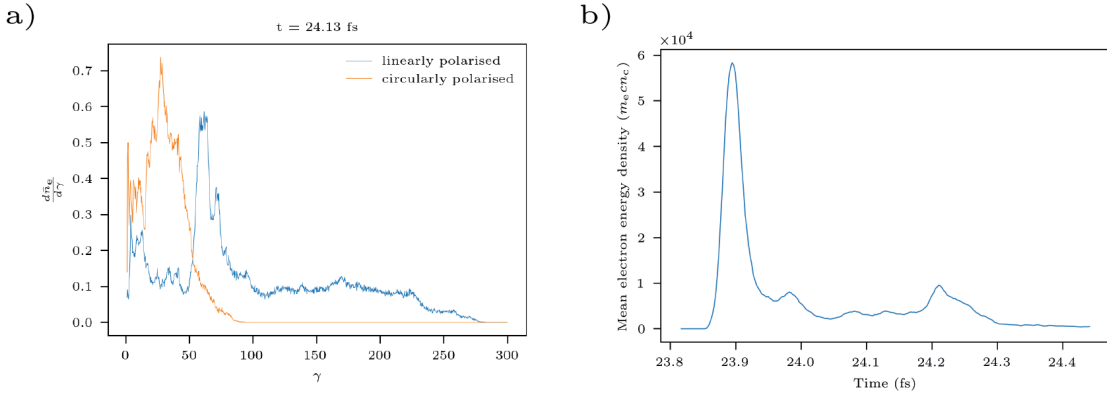


Figure 1.8: a) Energy spectra for mass-limited electron bunches formed via linearly and circularly polarised laser pulses. b) Mean energy density streaked in time through the centre of a mass-limited ZVP electron bunch demonstrating the attosecond duration.

be increased indefinitely and there is no limit to the mass-limited electron bunch total charge. For a realistic laser pulse with beam width 10λ incident on a larger plasma block, Equation 1.48 predicts a charge of 9.3 nC.

Figure 1.8a compares the electron bunch energy to an equivalent bunch produced by a circularly polarised laser pulse². The mean electron bunch energy is over three times lower as there is no ZVP acceleration phase and there is no quasi-monochromatic structure [14]. Figure 1.8b plots the mean electron bunch energy in time at a point as the bunch passes, clearly demonstrating the attosecond duration of the electron bunch.

Applications: from electron bunches to attosecond light

There are a plethora of applications for high charge, attosecond electron bunches, primarily for the purpose of resolving attosecond scale phenomena [33]. Already femtosecond pump, attosecond probe experiments are underway [34, 35] but the higher intensities and charge densities accessible in the laser-solid regime compared to in laser-gas interactions [9, 24] would represent a step-change in the field by enabling atto-pump atto-probe experiments [5]. Potential applications include: electron microscopy and atomic diffraction to temporally resolve photoelectric processes such as Bragg diffraction [36], ultra-fast electron radiography to probe the

²A circularly polarised laser pulse will expel electrons from a mass-limited target in a corkscrew shape, the bunch is therefore only loosely equivalent.

evolution of the formation of magnetic fields in dynamical systems [37] or for XFEL seeding [10]: the record XFEL X-ray pulse duration stands at 280 attoseconds [38], substantially longer than the durations accessible using this technique. Electron bunches are also a promising alternative for radiotherapy due to their superior penetration depth in biotissues compared to X-rays [39].

Analogously to the HHG process, rapid acceleration of an electron bunch generates a burst of radiation whose properties (brightness, coherency, duration, spectrum) are determined by the corresponding properties of the electron bunch (charge, emittance, duration and energy). Thus globally electron bunches are used as a diagnostic tool in synchrotrons and XFELs. Other acceleration mechanisms for X-ray generation include: bremmstrahlung radiation from firing the electron bunch at a secondary high- Z target [40], interaction with a counter-propagating laser pulse [41, 42] or injection into a laser or plasma wakefield accelerator, including accessing the solid density plasma wakefield regime [9]. The mass-limited electron bunches produced via the ZVP mechanism have transverse emittances comparable in all planes to those conditioned in state-of-the-art nano-Coulomb electron bunch accelerators [43, 44]. Such facilities typically produce electron bunches with geometric emittances of \sim mm rad prior to damping ring injection [45] and \sim nm rad post-injection [43]. Thus, the mass-limited ZVP electron bunches are ideal candidates for the production of bright X-rays of unprecedentedly short duration and are suitable for study in the new attosecond regime with applications to physical, chemical and biological systems.

Parameter scan of electron bunch mean energy

It is important to confirm that mass-limited electron bunches follow the same scaling relations as has previously been confirmed for bulk ZVP electrons in both 1D [14] and 2D [13] PIC simulations. The mean mass-limited electron bunch kinetic energies were extracted from 120 2D PIC simulations and are plotted in Figure 1.9. The dependence of the energy on both a_0 and \bar{n}_e is immediately apparent and therefore these electron bunches are accelerated by a non-ponderomotive mechanism.

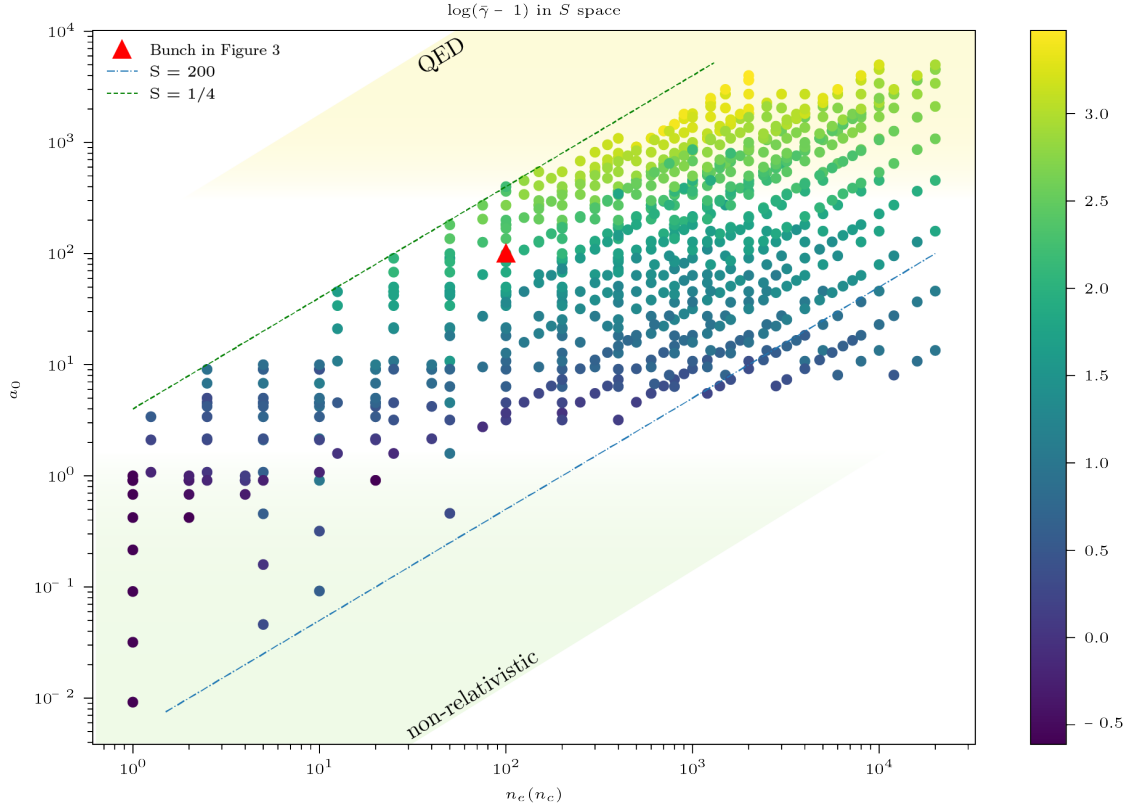


Figure 1.9: Mean mass-limited ZVP electron bunch normalised kinetic energies extracted from 2D PIC simulations. The bunch detailed in Figure 1.7 is highlighted.

The parameter scan took plasma block densities ranging from the critical plasma density to well-beyond solid density for the aluminium target and with laser pulse peak intensities ranging from non-relativistic ($a_0 < 1$) through to the Quantum Electro-Dynamics (QED) plasma regime ($a_0 > 300$) up to a peak $a_0 = 5000$ to investigate the change in scaling observed by Savin *et al* [25] at the onset of QED effects. This study is also the first to extract specific bunch energies as opposed to total simulation box energy gain, representing a far more precise test of ZVP theory. Particle merging was turned on for macro-photons and macro-electrons for $a_0 \geq 1800$ to prevent overloading of the available supercomputer memory due to the vast number of particles produced in this SF-QED regime.

A total of 856 data points for mass-limited electron bunch mean energies were extracted from the simulations. Bunches are arranged in trains with an average length of 4, however isolated bunches are more useful for attosecond diagnostics. The number of bunches in a given train as a function of simulation peak intensity and

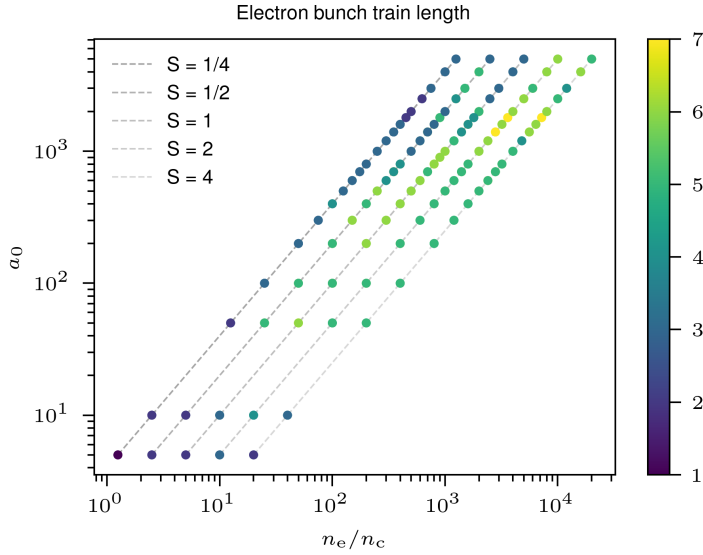


Figure 1.10: Mass-limited electron bunch train length as a function of laser intensity and plasma density. Lines of constant peak S parameter are plotted for reference. Clearly, decreasing S reduces the bunch length.

plasma density is plotted in Figure 1.10. It is clear that reducing the peak S reduces the train length. Where $S < 1$, the transition to relativistic self induced transparency occurs in the rising edge of the laser pulse corresponding to a breakdown of ZVP and an early cutoff to the bunch train. Other routes to isolated attosecond electron bunches can be likely borrowed from CSE theory given the close relation between the two. The interest in isolated attosecond pulse of radiation has led to the proliferation of ideas, suggested techniques include using the attosecond lighthouse technique using laser pulse wavefront rotation [46], few cycle laser pulses[47], non-collinear laser pulse gating [48] and circular polarisation gating [49].

Care must be taken as the energy of such electron bunches cannot be directly compared to the ZVP energy relations as as aforementioned, after escaping the potential, the electron bunch experiences further direct laser acceleration before reaching the detection point. Indeed, Thévenet *et al* [11] suggested that attosecond electron bunches produced in reflection exhibit precisely the phase and energy properties required to ‘surf’ the reflected laser pulse and experience vast acceleration gradients over the Rayleigh length of the laser pulse. This process is known as Vacuum Laser Acceleration. It seems highly likely that this process occurs for

electron bunches produced in transmission. This seemingly unfortunately situation in reality provide a fully optical scheme to create GeV nano-Coulomb electron bunches from the most basic of setups: a laser and a solid density target.

Returning to the determination of the electron bunch energy at the measurement point, consider now the journey of the electron bunch after expulsion from the plasma bulk. It is rotated back towards the plasma bulk by the magnetic field of the subsequent peak of the laser pulse, then travelling at approximately c it surfs the peak, experiencing an approximately constant accelerating electric field from the laser pulse at some fraction f of the laser field peak. The work done by this field is then

$$\Delta T = \int e\mathbf{E} \cdot d\mathbf{x}. \quad (1.49)$$

Note that for this process, the laser pulse electric field and electron bunch direction of travel will always be aligned no matter to which side of the plasma bulk the electrons are accelerated to and therefore ΔT will always increase the energy of the electron bunch, thus,

$$\Delta T = efE_L\Delta y, \quad (1.50)$$

where Δy is the distance along y from the plasma edge to the detection point. Accounting for the Gaussian spatial profile of the laser, $a(t) = a_0 \exp(-y^2/(6\lambda)^2)$ at focus, the gamma factor after both acceleration phases for this simulation setup is then

$$\gamma = 1 + (0.30) \times \frac{a_0^2}{\bar{n}_e} + (1.2f) \times a'_0. \quad (1.51)$$

Here the primed vector potential refers to the intensity of the subsequent peak of the laser pulse. This final term could be neglected or at least reduced somewhat once super-Gaussian spatial laser pulses become standard in this intensity regime or by using a suitable plasma separator [50], as applied in [51]. Both acceleration phases fail to meet the criteria of the Lawson-Woodward theorem. The ZVP phase is dependent on the existence of electrostatic forces, while the secondary phase occurs for a finite interaction region.

Fitting Equation 1.51 to the PIC simulation data presented in Figure 1.9 finds

$$\gamma = 1 + (0.46 \pm 0.02) \times \frac{a_0^2}{n_e} + (0.28 \pm 0.01) \times a'_0 \quad (1.52)$$

with an r^2 -value of 0.818. This fit suggests $f = 0.22 \pm 0.01$. The electric field experienced for a random selection of electrons in a bunch was extracted from one simulation. Encouragingly, the mean attenuation of the electric field they experience is 0.20 ± 0.05 , to calculate this attenuation directly falls beyond the scope of ZVP theory.

This is the first demonstration of ZVP theory to calculate absolute values and not only the scaling relationship. Such order of magnitude calculation is essential to compare this model of absorption to others and thus determine the dominant mode for absorption. It is certainly remarkable that such a simple theory for energy absorption has such predictive success in this highly non-linear and seemingly chaotic many particle system. It is interesting that increasing laser intensity to such extremes will, at least for a short time, cause relativistic effects that simplify the dynamics before the total annihilation of a target.

The relative error between data and theory is plotted in Figure 1.11. Those points marked by an orange triangle have associated errors of over an order of magnitude. Reassuringly, such points occur only after the onset of QED effects, known to impact the ZVP mechanism [25] and for $S < 1$, that is, where the plasma becomes relativistically transparent to the laser pulse, a fundamentally different regime. Equally, for non-relativistic laser intensities, where assumptions of electron coherency cannot be made, are poorly fit by the model. It is particularly interesting that there is no indication that large S causes a breakdown of the model, extending the applicability of the model further than previously considered and opening up the field to a wider range of conditions, such as that of shock compressed plasmas. To summarise, it would appear the ZVP model is valid for $10 \leq a_0 \leq 300$ and $S \geq 1$.

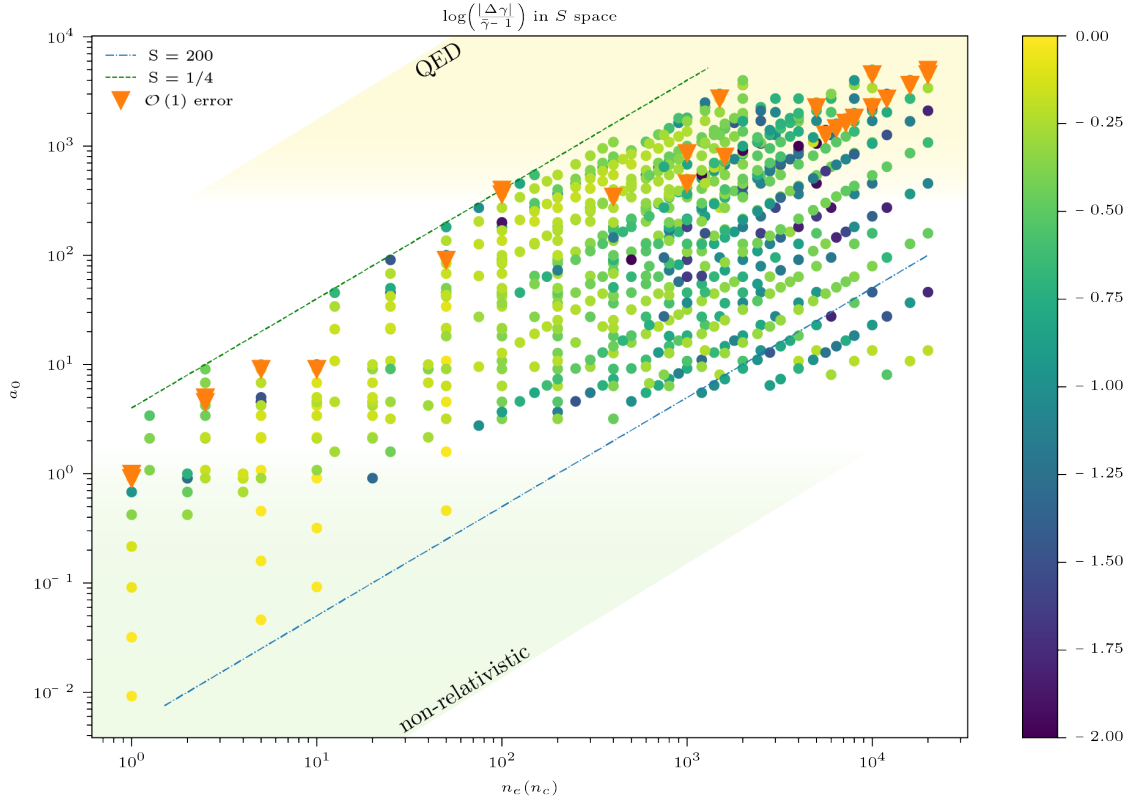


Figure 1.11: The relative errors for each mean energy data point compared to Figure 1.9. The orange triangles indicate data points for which the model fails to predict the mean energy.

1.4.1 Energy absorption in the ZVP regime

As stated previously the laser-plasma coupling exists in a state of adiabaticity with the exception of the ZVP acceleration phase and hence Equation 1.29 describes the absorption of laser pulse energy. As two bunches are produced per laser pulse cycle, the rate of energy transfer is therefore

$$R = \frac{U\omega_L}{\pi}, \quad (1.53)$$

for normal incidence. To observe the scaling for U in 2D PIC simulations, peak instantaneous electron bunch energies escaping to the rear of the bulk were extracted from those PIC simulations with $S = 1$. For constant S ,

$$U \sim a_0^2. \quad (1.54)$$

Energies are plotted in Figure 1.12. Fitting the total energy within the range of

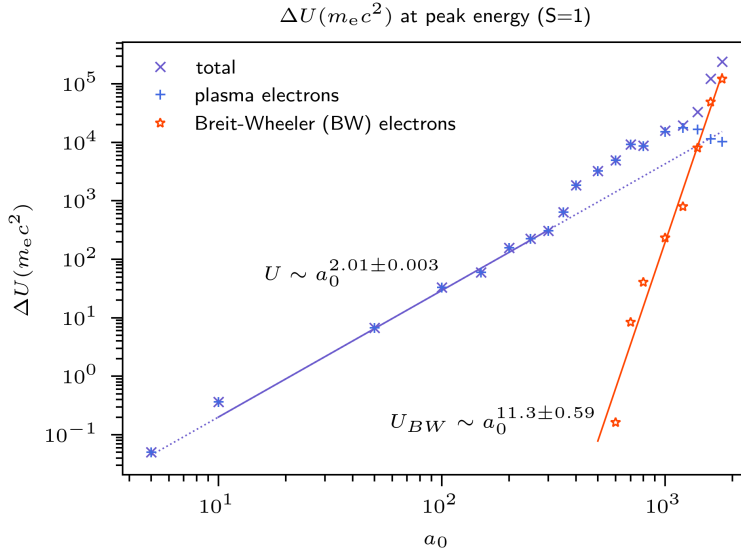


Figure 1.12: Peak instantaneous bulk electron bunch total energies after escaping to the plasma bulk rear. Energies begin to deviate from the anticipated scaling at approximately $a_0 = 300$. Above $a_0 = 1000$, BW pair produced electrons begin to dominate and the peak energies rise rapidly.

validity established for the ZVP model finds

$$U \sim a_0^{2.01 \pm 0.003}, \quad (1.55)$$

reproducing with great success the anticipated scaling within the ZVP regime. It is satisfying that the number of electrons and bunch mean energies both follow their anticipated ZVP scalings. It was not possible to reproduce the constants of Equation 1.29 as the neutralising return current in the plasma bulk generates an electrostatic field on the rear side of the plasma block, decelerating bulk electron bunches as they escape the plasma. It should be possible to calculate the deceleration by considering the number of electrons expelled by the plasma. It is, however, clear from the simulations that at least some electrons in the escaping bunch are trapped by this rear-side potential well reduces its ability to slow electrons.

While Equation 1.29 describes energy absorption into hot electron bunches, the coupling of such hot collisionless electrons to the bulk plasma given the lack of collisionality is naturally indirect. There are two key mechanisms [52]. Firstly, via a cooler resistive return current of electrons that neutralises the current of the injected

hot electrons that escape the potential well of the front surface. Since all hot electrons travel at approximately speed c , the magnitude of the return current depends not on the total energy absorbed but instead on the total number of electrons injected, as given by Equation 1.28, depending linearly on laser spot area and the electric field magnitude and not on the plasma density³. Secondly, via the formation of large amplitude bulk plasma waves induced in the wake of the hot electron bunches. Sherlock *et al* [52] calculate the magnitude of the induced wakefield to be

$$E_W = \frac{eN_e c}{\omega_p \epsilon_0} = \sigma \sqrt{\frac{m_e \epsilon_0}{n_e}} E_L, \quad (1.56)$$

where here the bunch velocity has been set to c , bulk electrons will be accelerated by E_W and their kinetic energy converted to heat via collisions. Interestingly, this reproduces the mid temperature electron scaling with density that was observed by Chrisman *et al* [53] in their study of hot electron energy coupling in cone-guided fast ignition of inertial fusion targets. This is a different possible explanation to their self-declared ‘hand waving argument’. Excluding this study, such formulations for heat transfer to the plasma bulk within the ZVP regime remain untested in simulations.

Note also that as the laser pulse intensity rises, the fraction of energy absorbed by the ion species increases. Savin [15] determined for $S = 1/2$, $a_0 = 100$, that this would be almost 20%. Energy is absorbed by ions via the hole boring mechanism as described later in this Thesis.

1.4.2 Unpacking the QED effects of Figure 1.12

In Savin’s acclaimed paper [25], they determined theoretically and demonstrated in simulation that at $a_0 = 300$, $n_e = 50n_c$, there is a transition from standard ZVP scalings to an enhanced QED scaling associated with Breit-Wheeler (BW) electrons increasing the pseudocapacitor plate charge. Explicitely,

$$T \sim \frac{a_0^5}{\bar{n}_e}. \quad (1.57)$$

³Note that for a sufficiently thin target, the return current induces an electrostatic field on the back surface of the target which can then reflect hot electron bunches and decelerate them to the point of a return to collisionality. This is a reality for the PIC simulations explored in this thesis, however, since realistic targets are much thicker this shall be neglected.

At first glance of Figure 1.12, Savin’s results are inconsistent with this parameter scan. Perhaps the measurement method can explain this via to the well known effect of radiation trapping from to Radiation Reaction (RR) [54], also observed in these PIC simulations. After acceleration across the pseudocapacitor, the electron bunch encounters the subsequent laser peak. If the electron bunch gamma factor and laser intensity are both large enough, electrons radiate a significant fraction of their energy and are thus stopped in their tracks. Unable now escape the potential well at the plasma surface they are trapped and are not observed to escape the plasma until the laser pulse intensity reduces. Such an effect would not impact Savin’s scalings but would of course inhibit the observation of the scaling for electrons rear of the plasma block. Note that should this be the case and the collisionless electron bunches remain within the plasma bulk, Savin’s ZVP QED model truly applies directly to energy absorption by the plasma bulk.

There is another interpretation. Returning now to Figure 1.12, there are two interesting aspects. Firstly, the sudden jump in total energy at $a_0 \approx 300$. This cannot be explained by ZVP theory nor QED theory since the jump is observed with QED effects switched off. Secondly, the even sharper jump in total electron bunch energy above $a_0 = 1000$. Decomposing the total energy into bulk electrons and those produced via the BW process, this is clearly a QED effect. Energy in BW produced electrons scales at a staggering

$$U_{\text{BW}} \sim a_0^{11.3 \pm 0.8}, \quad (1.58)$$

while the energy of bulk plasma electrons decreases. Perhaps this is a signal of Savin’s QED ZVP electron bunches only at a higher energy due to the substantially greater plasma density of these simulations. The reduction in bulk electron energy can be attributed to an oversaturation of the front surface with BW electrons.

Combining equations ?? and 1.29 and assuming the electron radiates all its energy to the photon, for the ZVP mechanism, at the point of emission one finds

$$\chi_\gamma = \frac{\sqrt{2}|\mathbf{E}|}{E_S} \frac{a_0^2}{\bar{n}_e}. \quad (1.59)$$

The probability of BW pair production begins to rapidly increase around $\chi = 1$, therefore, the transition to QED will occur at

$$a_0 \approx \left(\frac{E_S}{\sqrt{2}} \frac{e\bar{n}_e}{m_e c \omega_L} \right)^{1/3} = \left(\frac{a_s \bar{n}_e}{\sqrt{2}} \right)^{\frac{1}{3}}, \quad (1.60)$$

where $a_s = 7.73 \times 10^5$ is the normalised vector potential associated with the Schwinger Field. Repeating the calculation instead as a function of S , one finds instead

$$a_0 \approx \left(\frac{a_s S}{\sqrt{2}} \right)^{\frac{1}{2}}. \quad (1.61)$$

This corresponds to a transition to rapid pair production with Savin's parameters of $a_0 \approx 301$ versus $a_0 \approx 739$, consistent with both studies. This is interesting, ZVP with Savin parameters predicts a significantly lower transition to QED compared to the Wilks scaling for $\mathbf{J} \times \mathbf{B}$ heating. Following Savin's QED ZVP theory, one can predict

$$U_{\text{QED}} \sim \frac{a_0^7}{S}, \quad (1.62)$$

therefore much work remains understand the scaling of Figure 1.12 and unify these results, starting with the application of the methods of this analysis to the parameter space explored by Savin. Undoubtedly, the advent of next generation exa-watt scale lasers and access to this regime will be exceedingly interesting if such scalings in bunch energy can be maintained.

Linear Breit-Wheeler can safely be neglected in these simulations. There is simply not enough energy in the system. For two interacting photons of energy E_1 , E_2 , by consideration of four-momenta, the threshold condition for pair production is

$$E_1 E_2 \geq (m_e c^2)^2. \quad (1.63)$$

For a near-infrared laser photon of energy $\hbar\omega_L$, the interacting photon must have an energy in excess of 200 GeV. Despite the extreme acceleration gradients considered in this thesis, the ZVP mechanism predicts photons of energies no greater than 10 GeV and thus linear Breit-Wheeler is suppressed.

He *et al* [55] identified an alternative mechanism for linear BW using solid density targets, where forwards- and back-scattered high energy radiation reaction

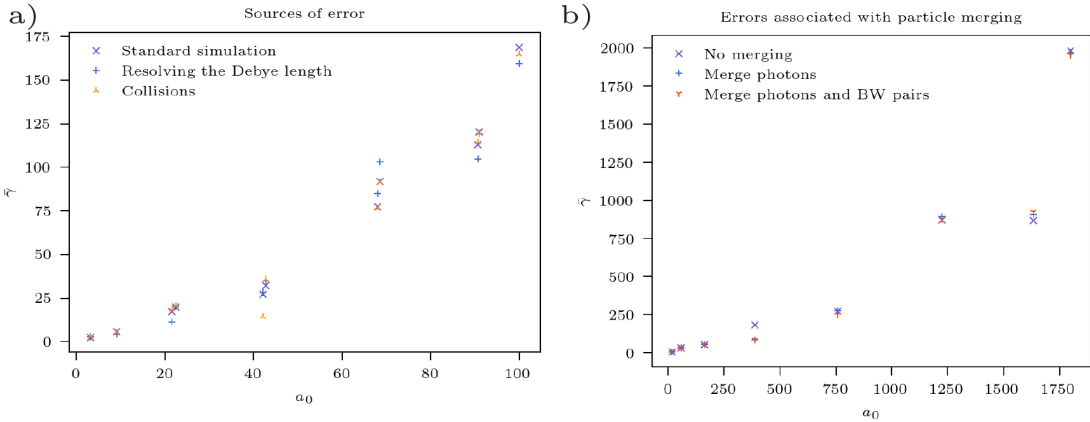


Figure 1.13: An exploration of ZVP 2D PIC simulation stability and assumptions. a) Electron bunch mean energies extracted from simulations with a_0 , $\bar{n}_e = 100$. Here, the x -axis is the normalised vector potential of the laser pulse cycle that made them, this is why there appears to be results stacked. b) Electron bunch mean energies extracted from simulations with a_0 , $\bar{n}_e = 1800$ both with and without particle merging.

produced photons interact within a hollowed out plasma channel. In the geometry of interest in this thesis, while photons are produced in both directions, their production is localised to the plasma surface and at no points do their paths cross and thus this mechanism does not occur.

1.4.3 Errors

A set of simulations were undertaken to explore the stability of some assumptions of the PIC simulations. The effect of including collisions, increasing the temperature to resolve the Debye length and particle merging were explored. The results are presented in Figure 1.13. In general including collisions had little to no effect on the results and changing the Debye length had a small but not systematic impact on the results. Note that while numerical heating is not directly dependent on laser intensity, increases to a_0 would increase the electron bunch density. Thus, resolving the Debye length of the ultra-high density (orders of magnitude greater than solid density) electron bunches produced by the higher laser pulse intensities considered here is no straightforward task. Particle merging was essential for simulations with $a_0 > 1800$ due to the proliferation of high energy photons and electron-positron

pairs. At least at $a_0 = 1800$ it would appear particle merging had negligible impact, however it is likely the error would increase with a_0 .

1.5 Planned future work

Simulations can only go so far. After a successful proposal application, five weeks of beam time have been awarded on the GEMINI-PW laser facility at the Central Laser Facility (CLF) [56]. This July, the study of mass-limited ZVP electron bunches will be put to the test as part of a three-pronged experimental campaign. The main experimental goals are

1. to characterise the X-ray HHG emission from the reflection of a relativistic laser off a solid target, following on from a March 2023 experiment at the ORION laser facility at AWE [57], which is discussed in great detail in the following Chapter;
2. to simultaneously measure and correlate HHG and the ZVP electron bunches using a novel experimental setup;
3. to apply the attosecond X-ray HHG beam as a diagnostic tool in a proof of principle warm dense matter experiment.

Preparations are now underway. The requirements for this experiment are simple: a relativistically intense high contrast laser pulse ($a_0 \geq 10$) of a few femtoseconds duration incident on a solid target with surface perturbations small compared to the wavelength of the laser pulse. A simulation describing the experimental setup for the ZVP bunch measurement is given in Figure 1.14. By focusing the laser onto the edge of a transversely mass-limited target, the emitted electron bunch energies will be maximised. Simulations suggest it should be possible to simultaneously measure the specularly reflected HHG and the attosecond electron bunches that produce it. Note via equations 1.47 and 1.26, the low density target of Figure 1.14 will produce larger and more energetic bunches. They are therefore a more practical choice for the experiment relative to the aluminium targets of previous sections

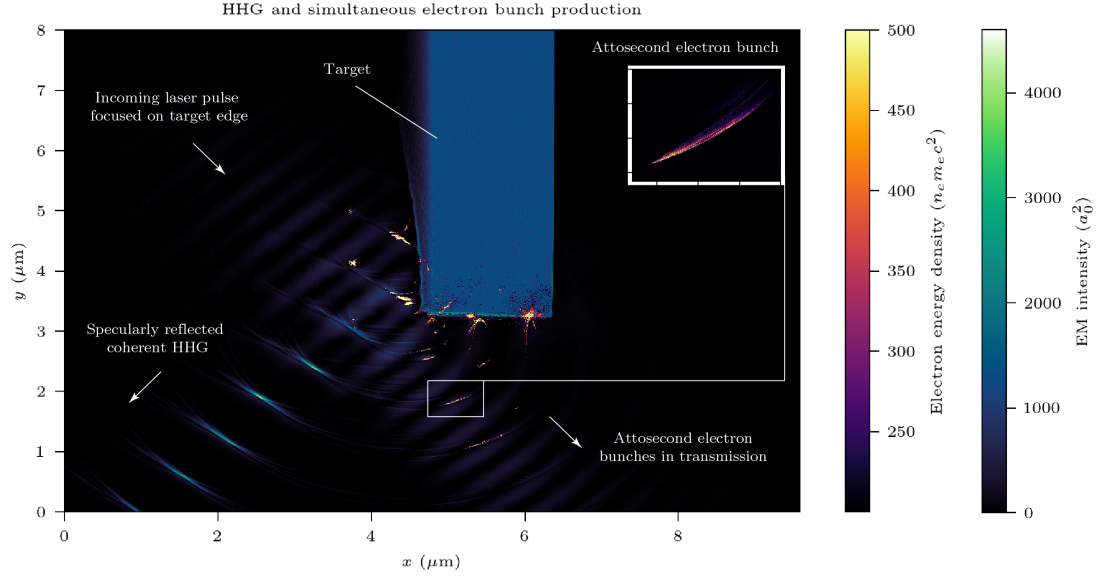


Figure 1.14: A simulation of the planned GEMINI-PW experimental setup for the measurement of ZVP electron bunches. This novel setup enables the simultaneous measurement of attosecond ZVP electron bunches and their coherent emission of X-ray light. The GEMINI-PW laser pulse is incident at 45° on the low density polyethylene target with a preplasma scale length of $0.2\lambda_L$. For this angle of incidence, transmitted bunches and specularly reflected X-ray harmonics are produced at a frequency of ω_L .

It is necessary to conduct PIC code parameter scans for this new geometry. While normal incidence was most convenient for initial simulations, oblique incidence is more optimal for HHG [16, 24] and as can be understood from equations 1.43 and 1.44, the new energy scaling expressions for the ZVP mechanism at oblique incidence. Not only is oblique preferable but it is essential to mitigate damage to the laser optics via back-reflection. The HHG beam intensity at focus can be over 1000 times that of the incident laser pulse [58]. It is necessary, therefore, to test the new predictions for oblique incidence energy scalings and total electron bunch charge as well as the angle of bunch ejection, the non-zero transverse vector potential of the laser will prevent the bunch from propagating directly along the transmission axis. It would also be useful to perform a parameter scan of preplasma scale length. In this work so far, it was assumed that the optima for electron bunch production are simply those for HHG given their intrinsic link.

GEMINI-PW laser facility

The GEMINI-PW laser facility housed at the CLF is a petawatt class facility consisting of two 30 fs beams each delivering a maximum focused intensity of $2 \times 10^{21} \text{ W cm}^{-2}$ at a repetition rate of 0.05 Hz. Such high frequency of operation has led to a paradigm shift in high power laser physics experimentation with the arrival of statistically significant results.

Targets

A range of thick, flat solid targets are proposed to probe the density parameter space: diamond, a selection of plastics (polymethyl methacrylate, low and high density polyethylene and polycarbonate) and mirrored targets, which produced interesting and slightly unexpected results in the ORION experiment. It would also be interesting to produce foam targets gaining access the optimal low S regime [59]. Target wheels will be used to take full advantage of the high shot rate of the GEMINI-PW laser.

For target edge shots, high edge precision is absolutely essential. To overcome this challenge we have designed 300 μm cryo-etched silicon targets with well-defined edges of micron precision. However, as we anticipate some relaxation in the requirement for such micron precision given the smoothing from preplasma expansion and the smoothing effect of the main pulse interaction as noted by Dromey *et al* [60], we will also explore tape drives as an option, however, considering the jitter of such devices, we anticipate a low success rate of $\sim 4\%$. This is not necessarily unreasonable. Shot-to-shot variations in laser pulse focal spot position are typically on the order of the focal spot itself. Therefore only a third of silicon target shots will be successful and will depend on the gathering of sufficient statistics as will be possible with the high repetition rate of the GEMINI PW laser facility. Successful shots will be identified using a third harmonic imaging line [60].

Diagnostics

The electron bunches will be measured using an electron spectrometer placed a few centimetres from the target to measure the time-integrated energy spectrum. The spectrometer will be shielded from the laser pulse and any HHG in transmission using a flash coated kapton foil which should not significantly hinder the MeV electron bunches produced in the interaction. Mordovanakis *et al* used Image Plate stacks to obtain the electron bunch structure and emission angle, it may be necessary to perform this first to accurately position the spectrometer [61]. While resolving attosecond durations remains a serious technical challenge of experimental science, we hope to measure the production of Coherent Transition Radiation from a secondary target and therefore infer the presence of a bunch train [9]. The X-ray HHG emission will be measured using a replica OHREX spectrometer [62], a spherically bent crystal spectrometer with ultra-high resolution and high-signal-to-noise ratio. Lower order harmonics will be measured using angularly resolved EUV spectrometers. Note that in the absence of attosecond resolution diagnostics, measuring the harmonic spectrum of the coherent HHG is the only way to reconstruct the temporal shape of the pulse. Simulations have suggested that the reflected spectrum produced by Coherent Synchrotron Emission of the electron bunches is approximately Fourier-limited [12]. A quarter wave plate could be used to convert the incoming laser pulse to a circular polarisation to compare the signals to those detected in the absence of zeros in the vector potential.

Preplasma scale lengths and prepulse control

Observation of the ZVP mechanism requires a sufficiently steep density gradients at the laser-plasma interface. An inevitable challenge of Chirped Pulse Amplification (CPA) laser systems is the existence of prepulses that heat targets, causing them to expand significantly before arrival of the main pulse. To increase the laser contrast, to the point where there is no preplasma formation, GEMINI-PW utilises a Double Plasma Mirror setup [63]. Each mirror is an anti-reflection coated optic placed in the path of the laser beam, acting as an optical switch. As the laser fluence

passes the damage threshold of the optic, plasma forms on the front surface and the mirror starts to reflect. Investigation of preplasma generation will occur in parallel to the main experimental goals.

1.6 Conclusions

The Zero Vector Potential mechanism describes the post-ponderomotive rapid absorption of ultra-relativistic laser energy by a solid density overdense, collisionless and fully ionised plasma on the timescales of ion immobility. The defining characteristics of the mechanism have been identified in 3D PIC simulations including the observation of a zero of the vector potential propagating at speed $\approx 1.4c$ through a high density ZVP electron bunch at the front surface of the plasma early in the ablative journey of the electron bunch. Simulations have suggested that from currently operational 10 PW short pulse laser facilities and foam targets, the ZVP mechanism can produce a train of attosecond duration, nano-Coulomb electron bunches, each with a transverse emittance of a few nm rad. Such charge and quality is comparable to state-of-the-art electron bunch accelerators but on paradigm shifting timescales. Such timescales being those on which atomic processes occur, these electron bunches could be manipulated to literally ‘shed light’ onto fundamental biological and chemical processes. Via a massive 2D PIC parameter scan the energies of such mass-limited electron bunches have been compared to those predicted by the ZVP model, identifying a range of validity for the model, specifically $a_0 > 10$, $S > 1$. These simulations were also used to confirm the energy absorption scaling in 2D up to and into the QED regime. Finally, details were provided on the planned GEMINI-PW experiment where ZVP electron bunches and ZVP absorption could be observed for the first time. On the theme of experimentation, the following Chapter will now switch gears from absorption to reflection for the discussion recent results from the ORION laser facility.

Appendices

A

General plasma physics

Contents

A.1	Lorentz transformations of electromagnetic fields	47
A.2	The headlight effect	48
A.3	Geometric transverse emittance	48

A.1 Lorentz transformations of electromagnetic fields

The Lorentz transformations for electromagnetic field components parallel, \parallel , and perpendicular, \perp , to a frame of reference boost of velocity \mathbf{v} are [23]

$$\mathbf{E}'_{\parallel} = \mathbf{E}_{\parallel}, \quad (\text{A.1})$$

$$\mathbf{B}'_{\parallel} = \mathbf{B}_{\parallel}, \quad (\text{A.2})$$

$$\mathbf{E}'_{\perp} = \gamma_{\mathbf{v}}(\mathbf{E}_{\perp} + \mathbf{v} \times \mathbf{B}), \quad (\text{A.3})$$

$$\mathbf{B}'_{\perp} = \gamma_{\mathbf{v}}(\mathbf{B}_{\perp} - \mathbf{v} \times \mathbf{E}/c^2). \quad (\text{A.4})$$

A.2 The headlight effect

The headlight effect describes the beaming of an isotropically emitting source travelling at some velocity relative to an observer. Consider the geometry of figure 1.2 with the source (the laser pulse) travelling at an angle 2θ to the observer (in this case, the ablating front). A photon with energy E emitted from the rest frame of the source (the laboratory frame in this case) has a 4-momentum

$$\mathbf{P}_\mu = \left(\frac{E}{c}, \frac{E}{c} \cos 2\theta, \frac{E}{c} \sin 2\theta \right). \quad (\text{A.5})$$

As the interaction geometry is confined to a 2D plane, the z -component can be safely neglected. Applying the lorentz boost of equation ??,

$$\begin{aligned} \frac{E'}{c} &= \gamma \left(\frac{E}{c} - \beta \frac{E}{c} \cos 2\theta \right) \\ \frac{E'}{c} \cos 2\theta' &= \gamma \left(\frac{E}{c} \cos 2\theta - \beta \frac{E}{c} \right). \end{aligned} \quad (\text{A.6})$$

Solving these equations for the angle in the boosted frame,

$$\cos 2\theta' = \frac{\cos 2\theta - \beta}{1 - \beta \cos 2\theta}. \quad (\text{A.7})$$

A.3 Geometric transverse emittance

A beam¹ of particles is fully described by its six-dimensional particle phase space distribution

$$\rho(\mathbf{x}, \mathbf{p}) = \rho(x, p_x, y, p_y, z, p_z), \quad (\text{A.8})$$

where $\mathbf{p} = p_x \hat{\mathbf{x}} + p_y \hat{\mathbf{y}} + p_z \hat{\mathbf{z}}$ is the canonical momentum [64]. Under the Hamilton formalism, for ideal conditions, the six-dimensional volume of the beam in this space, termed the *emittance*, arises as a conserved quantity and is therefore a useful quantity to describe the beam quality. (something to do with it affecting the ability to focus the beam?? check the papers) It is useful to rotate the coordinate system so as to align with the beam's propagation. The distribution can be written as

$$\rho(\mathbf{x}', \mathbf{p}') = \rho(x_L, p_L, x_T, p_T, x_{T'}, p_{T'}), \quad (\text{A.9})$$

¹In this section it is electron beams and not bunches that are referred to to demonstrate the generality of these concepts.

where L is longitudinal to the beam's propagation direction, and T and T' are two orthogonal directions transverse to the beam's propagation. Where discussed in this thesis, T' will unanimously refer to the z -direction, that is, the additional direction in 3D simulations, all such simulations are designed such that the z -direction is transverse to the beam propagation direction.

Recording a six-dimensional phase space in experiment is impossible while in simulations it is almost prohibitively costly in terms of data storage. Hence, it is common practice to project the distribution onto three orthogonal sub-spaces corresponding to each spatial axis, L, T and T' and compute the area on each. Note that since the electron beam is ultra-relativistic, all electrons propagate at approximately c and therefore it is the transverse and not the longitudinal emittance that describes the beam's quality. As a particle beam does not typically exist with well-defined borders, the area used to describe the emittance is restricted to an ellipse containing only the high-density core of the distribution. For a subspace i , where $i = T$ or T' , Floettmann *et al* [65] derive the *transverse normalised emittance* as

$$\epsilon_{n,rms}^i = \frac{1}{m_e c} \sqrt{\langle x_i^2 \rangle \langle p_i^2 \rangle - \langle x_i p_i \rangle^2}, \quad (\text{A.10})$$

where $\langle \rangle$ is the second central moment of the particle distribution,

$$\langle ab \rangle = \frac{\int ab\rho(\mathbf{x}', \mathbf{p}')dV}{\int \rho(\mathbf{x}', \mathbf{p}')dV} - \frac{\int a\rho(\mathbf{x}', \mathbf{p}')dV \int b\rho(\mathbf{x}', \mathbf{p}')dV}{(\int \rho(\mathbf{x}', \mathbf{p}')dV)^2}, \quad (\text{A.11})$$

here $dV = \Pi_j dx_j dp_j$ for $j = L, T, T'$.

When working with emittances, most frequently in the literature it is the *transverse geometric emittance*, ϵ_{rms}^i that is discussed. This is a natural consequence of it being more readily accessible in experiments [64]. The geometric and normalised emittances are related via

$$\epsilon_{rms}^i = \frac{\epsilon_{rms}^i}{\gamma \beta_L}, \quad (\text{A.12})$$

where $\gamma = 1/\sqrt{1-\beta^2}$ refers to the beam's mean energy and $\beta_L \approx c$ is the ultrarelativistic beam's longitudinal speed.

The Courant-Snyder invariant which describes the ellipse that corresponds to the emittance is²

$$\epsilon_{\text{rms}}^i = \gamma x_i^2 + 2\alpha x x' \beta x_i'^2, \quad (\text{A.13})$$

here the coordinates are x_i and $x'_i = p_i/p_L$ [66]. The Twiss parameters are

$$\alpha = -\frac{\langle x_i x'_i \rangle}{\epsilon_{\text{rms}}^i}, \quad (\text{A.14})$$

$$\beta = \frac{\langle x_i \rangle}{\epsilon_{\text{rms}}^i} \quad (\text{A.15})$$

and

$$\gamma = \frac{\langle x_i'^2 \rangle}{\epsilon_{\text{rms}}^i}. \quad (\text{A.16})$$

Thus the shape of the ellipse and the divergence of the beam can be determined.

²Regrettably β and γ are the standard notations for the Twiss parameters, at all other locations in this thesis, these parameters will refer to the standard relativistic beta and gamma factors of objects respectively.

B

PIC simulations

Contents

B.1 Convergence of 3D PIC simulations	51
---	----

B.1 Convergence of 3D PIC simulations

To reduce the computation cost of the large 3D simulations, a lower resolution version of the original 3D simulation was performed. Results are presented in figure B.1, demonstrating reasonable convergence.

B.1. Convergence of 3D PIC simulations

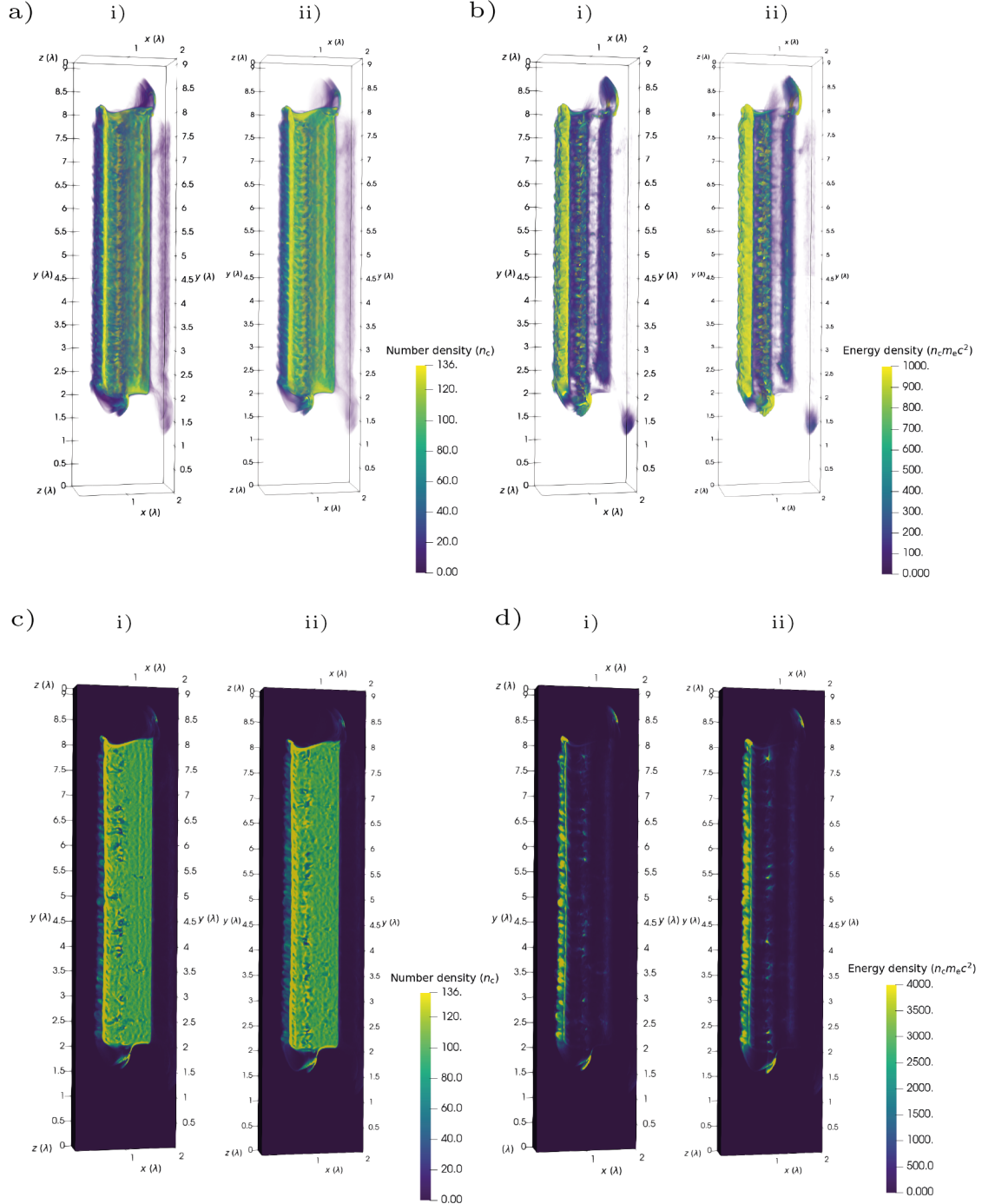


Figure B.1: Comparison between the initial 3D simulation and a lower resolution version. a) Electron number density. b) Kinetic energy density. c) and d) are slices of a) and b) respectively. *i*) Initial simulation. *ii*) Lower resolution simulation. Good convergence is demonstrated.

References

- [1] Victor V. Kulagin et al. “Characteristics of Relativistic Electron Mirrors Generated by an Ultrashort Nonadiabatic Laser Pulse from a Nanofilm”. In: *Physical Review E* 80.1 (July 13, 2009), p. 016404. URL: <https://link.aps.org/doi/10.1103/PhysRevE.80.016404> (visited on 08/31/2023).
- [2] Li-Xiang Hu et al. “Enhanced Dense Attosecond Electron Bunch Generation by Irradiating an Intense Laser on a Cone Target”. In: *Physics of Plasmas* 22 (Apr. 6, 2015), p. 033104.
- [3] Giada Cantono et al. “Extensive Study of Electron Acceleration by Relativistic Surface Plasmons”. In: *Physics of Plasmas* 25.3 (Mar. 1, 2018), p. 031907. arXiv: 1802.05483 [physics]. URL: <http://arxiv.org/abs/1802.05483> (visited on 08/31/2023).
- [4] D. A. Serebryakov, E. N. Nerush, and I. Yu Kostyukov. “Near-Surface Electron Acceleration during Intense Laser-Solid Interaction in the Grazing Incidence Regime”. In: *Physics of Plasmas* 24.12 (Dec. 1, 2017), p. 123115. arXiv: 1708.09833 [physics]. URL: <http://arxiv.org/abs/1708.09833> (visited on 08/31/2023).
- [5] Y. X. Zhang et al. “Giant Isolated Attosecond Pulses from Two-Color Laser-Plasma Interactions”. In: *Physical Review Letters* 124.11 (Mar. 18, 2020), p. 114802. URL: <https://link.aps.org/doi/10.1103/PhysRevLett.124.114802> (visited on 08/31/2023).
- [6] Vojtěch Horný and László Veisz. “Generation of Single Attosecond Relativistic Electron Bunch from Intense Laser Interaction with a Nanosphere”. In: *Plasma Physics and Controlled Fusion* 63.12 (Dec. 1, 2021), p. 125025. URL: <https://iopscience.iop.org/article/10.1088/1361-6587/ac2996> (visited on 10/03/2023).
- [7] J. F. Ong, P. Ghenuche, and K. A. Tanaka. “Electron Transport in a Nanowire Irradiated by an Intense Laser Pulse”. In: *Physical Review Research* 3.3 (Sept. 17, 2021), p. 033262. URL: <https://link.aps.org/doi/10.1103/PhysRevResearch.3.033262> (visited on 08/31/2023).
- [8] Victor V. Kulagin et al. “Subrelativistic Infrared and Terahertz Pulses from Petawatt Class Laser Interaction with Complex Nanodimensional Targets”. In: *Relativistic Plasma Waves and Particle Beams as Coherent and Incoherent Radiation Sources IV. Relativistic Plasma Waves and Particle Beams as Coherent and Incoherent Radiation Sources IV*. Ed. by Dino A. Jaroszynski and MinSup Hur. Online Only, Czech Republic: SPIE, Apr. 18, 2021, p. 11. URL: <https://www.spiedigitallibrary.org/conference-proceedings-of->

- [spie/11778/2592645/Subrelativistic--infrared-and-terahertz-pulses-from-petawatt-class-laser/10.1117/12.2592645.full](https://spie.org/Catalog/Detail?PaperID=2592645&PageNumber=1&PageCount=1&SectionID=11778&CategoryID=11778&PageType=FullText&PageFormat=PDF&PageName=Subrelativistic--infrared-and-terahertz-pulses-from-petawatt-class-laser&PageTitle=Subrelativistic--infrared-and-terahertz-pulses-from-petawatt-class-laser&PageURL=/11778/2592645/Subrelativistic--infrared-and-terahertz-pulses-from-petawatt-class-laser/10.1117/12.2592645.full) (visited on 08/31/2023).
- [9] Jinpu Lin et al. “Towards Isolated Attosecond Electron Bunches Using Ultrashort-Pulse Laser-Solid Interactions”. In: *Scientific Reports* 10.1 (1 Oct. 27, 2020), p. 18354. URL: <https://www.nature.com/articles/s41598-020-75418-6> (visited on 08/31/2023).
 - [10] D. E. Cardenas et al. “Sub-Cycle Dynamics in Relativistic Nanoplasma Acceleration”. In: *Scientific Reports* 9.1 (Dec. 1, 2019). pmid: 31086214.
 - [11] M. Thévenet et al. “Vacuum Laser Acceleration of Relativistic Electrons Using Plasma Mirror Injectors”. In: *Nature Physics* 12.4 (Apr. 1, 2016), pp. 355–360. arXiv: 1511.05936.
 - [12] S. Cousens et al. “Electron Trajectories Associated with Laser-Driven Coherent Synchrotron Emission at the Front Surface of Overdense Plasmas”. In: *Physical Review E* 101.5 (May 28, 2020), p. 053210. URL: <https://link.aps.org/doi/10.1103/PhysRevE.101.053210> (visited on 08/31/2023).
 - [13] A. F. Savin et al. “Attosecond-Scale Absorption at Extreme Intensities”. In: *Physics of Plasmas* 24.11 (Nov. 1, 2017).
 - [14] T. Baeva et al. “The Zero Vector Potential Mechanism of Attosecond Absorption”. In: *Physics of Plasmas* 18.5 (May 2011).
 - [15] Alex Savin. “Modelling Laser-Plasma Interactions for the Next Generation of High-Power Laser Experiments”. In: (2019).
 - [16] A. A. Gonoskov et al. “Ultrarelativistic Nanoplasmonics as a Route towards Extreme-Intensity Attosecond Pulses”. In: *Physical Review E* 84.4 (Oct. 10, 2011), p. 046403. URL: <https://link.aps.org/doi/10.1103/PhysRevE.84.046403> (visited on 07/24/2023).
 - [17] D. an Brügge and A. Pukhov. “Enhanced Relativistic Harmonics by Electron Nanobunching”. In: *Physics of Plasmas* 17.3 (Mar. 2010), p. 033110. arXiv: 1002.3576 [physics]. URL: <http://arxiv.org/abs/1002.3576> (visited on 08/31/2023).
 - [18] H. Vincenti et al. “Optical Properties of Relativistic Plasma Mirrors”. In: *Nature Communications* 5 (Mar. 11, 2014), p. 3403. pmid: 24614748.
 - [19] Andrea Macchi. “Theory of Light Sail Acceleration by Intense Lasers: An Overview”. In: *High Power Laser Science and Engineering* 2 (July 1, 2014), e10.
 - [20] S C Wilks et al. *Absorption of Ultra-Intense Laser Pulses*. 1992.
 - [21] Herbert Goldstein. *Classical Mechanics*. Pearson Education, 2013.
 - [22] T. Baeva, S. Gordienko, and A. Pukhov. “Theory of High-Order Harmonic Generation in Relativistic Laser Interaction with Overdense Plasma”. In: *Physical Review E - Statistical, Nonlinear, and Soft Matter Physics* 74.4 (2006). arXiv: physics/0604228.
 - [23] Andrew M. Steane. *Relativity Made Relatively Easy*. OUP Oxford, Oct. 4, 2012. 437 pp. Google Books: 75rCErZkh7EC.

- [24] Matthew R. Edwards and Julia M. Mikhailova. “The X-Ray Emission Effectiveness of Plasma Mirrors: Reexamining Power-Law Scaling for Relativistic High-Order Harmonic Generation”. In: *Scientific Reports* 10.1 (Dec. 1, 2020), p. 5154. pmid: 32198482.
- [25] Alex F. Savin et al. “Energy Absorption in the Laser-QED Regime”. In: *Scientific Reports* 9.1 (Dec. 1, 2019), p. 8956. pmid: 31222083.
- [26] Arkady Gonoskov. “Theory of Relativistic Radiation Reflection from Plasmas”. In: *Physics of Plasmas* 25.1 (Jan. 1, 2018). arXiv: 1708.05364.
- [27] A. Pukhov et al. “Relativistic High Harmonics and (Sub-)Attosecond Pulses: Relativistic Spikes and Relativistic Mirror”. In: *The European Physical Journal D* 55.2 (Nov. 2009), pp. 407–414. URL: <http://link.springer.com/10.1140/epjd/e2009-00187-4> (visited on 02/23/2024).
- [28] Matthew R. Edwards, Nicholas M. Fasano, and Julia M. Mikhailova. “Electron-Nanobunch-Width-Dominated Spectral Power Law for Relativistic Harmonic Generation from Ultrathin Foils”. In: *Physical Review Letters* 124.18 (May 8, 2020). pmid: 32441983.
- [29] J. Derouillat et al. “Smilei : A Collaborative, Open-Source, Multi-Purpose Particle-in-Cell Code for Plasma Simulation”. In: *Computer Physics Communications* 222 (Jan. 2018), pp. 351–373. URL: <https://linkinghub.elsevier.com/retrieve/pii/S0010465517303314> (visited on 08/15/2023).
- [30] K. A. Tanaka et al. “Current Status and Highlights of the ELI-NP Research Program”. In: *Matter and Radiation at Extremes* 5.2 (Mar. 1, 2020), p. 024402. URL: <https://pubs.aip.org/mre/article/5/2/024402/253013/Current-status-and-highlights-of-the-ELI-NP> (visited on 08/31/2023).
- [31] A. Bret, L. Gremillet, and M. E. Dieckmann. “Multidimensional Electron Beam-Plasma Instabilities in the Relativistic Regime”. In: *Physics of Plasmas* 17.12 (Dec. 1, 2010), p. 120501. URL: <https://pubs.aip.org/pop/article/17/12/120501/919014/Multidimensional-electron-beam-plasma> (visited on 08/31/2023).
- [32] F. Dollar et al. “Enhanced Laser Absorption from Radiation Pressure in Intense Laser Plasma Interactions”. In: *New Journal of Physics* 19.6 (June 1, 2017).
- [33] Ferenc Krausz and Misha Ivanov. “Attosecond Physics”. In: *Reviews of Modern Physics* 81.1 (Feb. 2, 2009), pp. 163–234. URL: <https://link.aps.org/doi/10.1103/RevModPhys.81.163> (visited on 08/31/2023).
- [34] F Calegari et al. “Ultrafast Electron Dynamics in Phenylalanine Initiated by Attosecond Pulses”. In: () .
- [35] Eiji J Takahashi et al. “Nonlinear Attosecond Metrology by Intense Isolated Attosecond Pulses”. In: *IEEE JOURNAL OF SELECTED TOPICS IN QUANTUM ELECTRONICS* 21.5 (2015).

- [36] Yuya Morimoto and Peter Baum. “Diffraction and Microscopy with Attosecond Electron Pulse Trains”. In: *Nature Physics* 14.3 (Mar. 2018), pp. 252–256. URL: <https://www.nature.com/articles/s41567-017-0007-6> (visited on 09/19/2023).
- [37] W Schumaker. “Ultrafast Electron Radiography of Magnetic Fields in High-Intensity Laser-Solid Interactions”. In: *Physical Review Letters* 110.015003 (2013).
- [38] Joseph Duris et al. “Tunable Isolated Attosecond X-ray Pulses with Gigawatt Peak Power from a Free-Electron Laser”. In: *Nature Photonics* 14.1 (1 Jan. 2020), pp. 30–36. URL: <https://www.nature.com/articles/s41566-019-0549-5> (visited on 08/31/2023).
- [39] Y. Glinec et al. “Radiotherapy with Laser-plasma Accelerators: Monte Carlo Simulation of Dose Deposited by an Experimental Quasimonoenergetic Electron Beam”. In: *Medical Physics* 33.1 (Jan. 2006), pp. 155–162. URL: <https://aapm.onlinelibrary.wiley.com/doi/10.1118/1.2140115> (visited on 09/19/2023).
- [40] S. Corde et al. “Femtosecond x Rays from Laser-Plasma Accelerators”. In: *Reviews of Modern Physics* 85.1 (Jan. 9, 2013), pp. 1–48. URL: <https://link.aps.org/doi/10.1103/RevModPhys.85.1> (visited on 08/31/2023).
- [41] K. Khrennikov et al. “Tunable All-Optical Quasimonochromatic Thomson X-Ray Source in the Nonlinear Regime”. In: *Physical Review Letters* 114.19 (May 14, 2015), p. 195003. URL: <https://link.aps.org/doi/10.1103/PhysRevLett.114.195003> (visited on 09/19/2023).
- [42] V V Kulagin, V N Kornienko, and V A Cherepenin. “Nonlinear Reflection of High-Amplitude Laser Pulses from Relativistic Electron Mirrors”. In: *Quantum Electronics* 46.4 (Apr. 30, 2016), pp. 315–320. URL: <http://stacks.iop.org/1063-7818/46/i=4/a=315?key=crossref.941653f9576f773499751dd5e2397e72> (visited on 08/31/2023).
- [43] Ian Martin. “Diamond Light Source Upgrade”. Low Emittance Ring Workshop (Frascati, Italy (Remote)). 2020.
- [44] He Ping. “The Progress of HEPS Project”. 8th Low Emittance Rings Workshop (Frascati, Italy (Remote)). 2020.
- [45] C Christou. “The Pre-Injector Linac for the Diamond Light Source”. In: *Proceedings of LINAC*. Lübeck, Germany, 2004, pp. 84–86.
- [46] H. Vincenti and F. Quéré. “Attosecond Lighthouses: How To Use Spatiotemporally Coupled Light Fields To Generate Isolated Attosecond Pulses”. In: *Physical Review Letters* 108.11 (Mar. 16, 2012), p. 113904. URL: <https://link.aps.org/doi/10.1103/PhysRevLett.108.113904> (visited on 12/23/2023).

- [47] P. Heissler et al. “Few-Cycle Driven Relativistically Oscillating Plasma Mirrors: A Source of Intense Isolated Attosecond Pulses”. In: *Physical Review Letters* 108.23 (June 6, 2012), p. 235003. URL: <https://link.aps.org/doi/10.1103/PhysRevLett.108.235003> (visited on 12/23/2023).
- [48] J P Kennedy, B Dromey, and M Yeung. “Isolated Ultra-Bright Attosecond Pulses via Non-Collinear Gating”. In: *New Journal of Physics* 24.11 (Nov. 1, 2022), p. 113004. URL: <https://iopscience.iop.org/article/10.1088/1367-2630/ac9b80> (visited on 12/11/2023).
- [49] M. Yeung et al. “Dependence of Laser-Driven Coherent Synchrotron Emission Efficiency on Pulse Ellipticity and Implications for Polarization Gating”. In: *Physical Review Letters* 112.12 (Mar. 26, 2014), p. 123902. URL: <https://link.aps.org/doi/10.1103/PhysRevLett.112.123902> (visited on 12/23/2023).
- [50] K. Miyauchi et al. “Laser Electron Acceleration by a Plasma Separator”. In: *Physics of Plasmas* 11.10 (Oct. 1, 2004), pp. 4878–4881. URL: <https://pubs.aip.org/pop/article/11/10/4878/261150/Laser-electron-acceleration-by-a-plasma-separator> (visited on 08/31/2023).
- [51] Alexander Andreev, Konstantin Platonov, and Saltanat Sadykova. “Double Relativistic Electron Accelerating Mirror”. In: *Applied Sciences* 3.1 (Feb. 4, 2013), pp. 94–106. URL: <http://www.mdpi.com/2076-3417/3/1/94> (visited on 08/31/2023).
- [52] M. Sherlock et al. “In-Depth Plasma-Wave Heating of Dense Plasma Irradiated by Short Laser Pulses”. In: *Physical Review Letters* 113.25 (Dec. 15, 2014).
- [53] B. Chrisman, Y. Sentoku, and A. J. Kemp. “Intensity Scaling of Hot Electron Energy Coupling in Cone-Guided Fast Ignition”. In: *Physics of Plasmas* 15.5 (May 1, 2008), p. 056309. URL: <https://pubs.aip.org/pop/article/15/5/056309/1016665/Intensity-scaling-of-hot-electron-energy-coupling> (visited on 09/06/2023).
- [54] L. L. Ji et al. “Radiation-Reaction Trapping of Electrons in Extreme Laser Fields”. In: *Physical Review Letters* 112.14 (Apr. 8, 2014), p. 145003. URL: <https://link.aps.org/doi/10.1103/PhysRevLett.112.145003> (visited on 09/07/2023).
- [55] Y He et al. “A Single-Laser Scheme for Observation of Linear Breit–Wheeler Electron–Positron Pair Creation”. In: *New Journal of Physics* 23.11 (Nov. 1, 2021), p. 115005. URL: <https://iopscience.iop.org/article/10.1088/1367-2630/ac3049> (visited on 10/02/2023).
- [56] *Laser System - Gemini.* UKRI STFC CLF. URL: <https://www.clf.stfc.ac.uk/Pages/Laser-system-Gemini.aspx>.
- [57] Nicholas Hopps et al. “Overview of Laser Systems for the Orion Facility at the AWE”. In: *Applied Optics* 52.15 (May 20, 2013), p. 3597. URL: <https://opg.optica.org/abstract.cfm?URI=ao-52-15-3597> (visited on 09/11/2023).

- [58] Fabien Quéré and Henri Vincenti. “Reflecting Petawatt Lasers off Relativistic Plasma Mirrors: A Realistic Path to the Schwinger Limit”. In: *High Power Laser Science and Engineering* (2021).
- [59] D. Batani et al. “Physics Issues for Shock Ignition”. In: *Nuclear Fusion* 54.5 (May 1, 2014), p. 054009. URL: <https://iopscience.iop.org/article/10.1088/0029-5515/54/5/054009> (visited on 09/18/2023).
- [60] B. Dromey et al. “Diffraction-Limited Performance and Focusing of High Harmonics from Relativistic Plasmas”. In: *Nature Physics* 5.2 (2009), pp. 146–152.
- [61] Aghapi G. Mordovanakis et al. “Quasimonoenergetic Electron Beams with Relativistic Energies and Ultrashort Duration from Laser-Solid Interactions at 0.5 kHz”. In: *Physical Review Letters* 103.23 (Dec. 1, 2009).
- [62] P. Beiersdorfer et al. “Lineshape Spectroscopy with a Very High Resolution, Very High Signal-to-Noise Crystal Spectrometer”. In: *Review of Scientific Instruments* 87.6 (June 1, 2016).
- [63] G. Doumy et al. “Complete Characterization of a Plasma Mirror for the Production of High-Contrast Ultraintense Laser Pulses”. In: *Physical Review E* 69.2 (Feb. 9, 2004), p. 026402. URL: <https://link.aps.org/doi/10.1103/PhysRevE.69.026402> (visited on 09/06/2023).
- [64] K. T. McDonald and D. P. Russell. “Methods of Emittance Measurement”. In: *Frontiers of Particle Beams; Observation, Diagnosis and Correction*. Ed. by M. Month and S. Turner. Vol. 343. Berlin/Heidelberg: Springer-Verlag, 1989, pp. 122–132. URL: <http://link.springer.com/10.1007/BFb0018284> (visited on 08/31/2023).
- [65] Klaus Floettmann. “Some Basic Features of the Beam Emittance”. In: *Physical Review Special Topics - Accelerators and Beams* 6.3 (2003), pp. 80–86.
- [66] Wiedemann. *Particle Accelerator Physics*. New York, NY: Springer Berlin Heidelberg, 2015.